Modeling A-Current Modulation in *Tritonia diomedea*

A Thesis
Presented to
The Academic Faculty

by

Naïm Richard Darghouth

In Partial Fulfillment
of the Requirements for the Degree
Master of Science

School of Electrical and Computer Engineering
Georgia Institute of Technology
May 2004

Modeling A-Current Modulation in *Tritonia diomedea*

Approved by:

Dr. Robert J. Butera, Principal Advisor

Dr. Paul S.Katz, Co-advisor

Dr. Robert Lee

Dr. Paul Hasler

May 12, 2004

TABLE OF CONTENTS

LIST OF TABLES

LIST OF FIGURES

ACKNOWLEDGEMENTS

First, I want to thank my family, who have always supported me in achieving my academic goals. *Merci Maman. Merci Papa.*

I feel very fortunate to have been advised by Dr. Robert Butera, from the school of Electrical and Computer Engineering at Georgia Institute of Technology, and Dr. Paul Katz, from the department of Biology at Georgia State University. It was a unique experience and an honor to have such exceptional advisors with distinct mentoring styles, complementing one another very nicely. Thank you.

I would also like to thank Dr. Akira Sakurai, a post-doc in the Katz lab. All the experimental data presented in this thesis was collected by Dr. Sakurai. He was also very helpful during our discussions of the project.

I would like to acknowledge the members of the Butera group, particularly Murat Şekerli, Liston Purvis, Paul Garcia, and Amanda Preyer, with whom I have had fruitful discussions throughout my thesis research.

Finally, I would like to thank my great friends Kofi Odame, WeiFeng Li, and $(\text{Buford})^{-1}$ for their support and presence in the past two years.

SUMMARY

This study uses a conductance-based computer simulation to test the feasibility of a mechanism underlying a newly-described dynamic form of neuromodulation, called spike-timing dependent neuromodulation (STDN). In the mollusc, *Tritonia diomedea*, it was recently found that a serotonergic neuron (called DSI) alters the synaptic strength of another neuron (VSI-B) in a temporally biphasic-bidirectional manner, with an initial potentiation followed by prolonged synaptic depression [43]. Physiological evidence suggested that the depression phase is due to serotonin enhancing the A-current in VSI-B, thereby causing spike-narrowing or a decrease in spike amplitude, and thus a decrease in transmitter release. We sought to test the feasibility of this mechanism by developing a conductance-based model of VSI-B using a Hodgkin-Huxley style simulation with a minimal number of ion conductances: A-current, delayed rectifier potassium, fast sodium, and leak channels.

From our model, we conducted simulations in order to study how the spike shape of the VSI-B action potential changes as the A-current conductance is enhanced, from which we are able to predict the amount of depression in the post-synaptic cell. Our model indicates that the depression due to the narrowing of the spike with A-current enhancement is sufficient to account for the empirically observed depression during STDN, although it suggests a greater effect of serotonin at the terminals than is observed in the soma. Additionally, the model suggested that the slow inactivation kinetics of the A-current cannot explain the dynamics of the depression phase of STDN. These modeling results suggest that serotonergic modulation of the A-current plays a role in STDN but does not account for its dynamics.

CHAPTER I

INTRODUCTION

The advent of mathematical neuronal modeling with Hodgkin and Huxley's squid axon model in 1952 added a dimension to traditional electrophysiology [25]. Extracted parameters from empirical data can be fit to curves and incorporated into a computational model which reproduces essential characteristics of electrical activity in neurons. A computer model of a neuron can serve the following purposes:

1. Neuronal models can be used to integrate experimental results into a precise mathematical description. By doing so, we can use the model as a tool for understanding the mechanisms underlying experimental observations and test a specific hypothesis that might have been developed from the empirical results. Though a model cannot prove the existence of a mechanism or confirm a hypothesis, it can provide evidence of feasibility (or infeasibility) for a hypothesized mechanism. For example, the first mathematical description of a neuron (the giant squid axon model) showed that the sodium, potassium, and leak currents were sufficient to accurately reproduce the electrical properties of that neuron [25]. It also gave a probable explanation of how the nonlinear voltage-sensitive ionic conductances interact with one another during neuronal activity.

2. Neuronal models can be used to transcend the limitations of traditional electrophysiological techniques, by simulating experiments which are not practicable in "real" conditions. As opposed to experiments, we have full control over the simulations. For example, we can use models to completely block specific currents without side effects. Most pharmacological ion channel blockers, such as tetraethylammonium (TEA) or 4-aminopyridine (4-AP), are not fully effective

in neurons (they cannot achieve a perfect block) and have side effects, such as an increase in leak conductance. Additionally, models enable us to track specific variables during activity that may not be experimentally observable. In the current study for example, we are interested in studying the amount of A-current during neuronal activity, which could only be done using a model.

3. In some cases, neuronal models are developed to run a large number of experiments in a limited amount of time. As computer processor time is relatively inexpensive compared to human time, it is advantageous to use computer simulations to sweep through a large number of parameters, for example, which might take a few hours on a computer compared to a few weeks or even months through experiments.

4. We can develop hypotheses from neuronal models, which may provide direction for future experimental work. In this case, one can use *experiments* to test predictions made by *models*. This is less common than the reverse, but models have been used in this manor previously [6].

In this study, we have developed a Hodgkin-Huxley style circuit model of a neuron to provide evidence of feasibility for a hypothesis developed from empirical studies of a newly described form of heterosynaptic neuromodulation, spike-timing dependent neuromodulation (STDN). Experiments conducted on neurons from the central pattern generator (CPG) circuit controlling swimming in *Tritonia diomedea* have suggested that the depression phase of STDN is mediated by the release of serotonin (5-HT) from a serotonergic neuron which indirectly enhances a transient potassium current (A-current). The enhancement of an outward current is thought to lead to a narrowing in spike shape, which in turn would lead to less neurotransmitter release from the neuron and depression in its evoked excitatory post-synaptic current (EPSC). By modeling the A-current from empirical voltage clamp data, we are able

to test how this conductance may affect spike shape and hence the amplitude of the evoked synaptic current.

In chapter 2, we will present background and contextual information related to the study. Next, we will outline the neuronal modeling methods used for constructing our neuronal model in chapter 3. We will then describe how the A-current and the neuron was modeled to fit experimental data, as well as the results of simulations testing our principle hypothesis using our model, in chapter 4. A discussion of the implications of our results and conclusions drawn from them will be presented in chapter 5.

CHAPTER II

BACKGROUND AND CONTEXT

2.1 Neuromodulation

Neuromodulation alters the activity of neurons by enhancing or reducing their synaptic strength, and plays an essential role in central pattern generator (CPG) circuits [30]. Neurons that are external to a neuronal circuit can modify the circuit via neuromodulation to have different functional configurations; this is called extrinsic neuromodulation. Neuromodulation originating from a neuron inside the neuronal circuit which is essential for circuit functioning is called intrinsic neuromodulation [9, 34]. The function and significance of extrinsic neuromodulation to neuronal circuits has been established and is well defined [21, 32, 26, 34]; it has the capability of reconfiguring a neuronal circuit to serve different roles. The second type of neuromodulation is less well understood, as its dynamics can be complex and interrelated with the traditional neurotransmission mechanisms of the neuronal circuit [34]. In the last 15 years, a number of central pattern generator (CPG) circuits have been identified as having intrinsic neuromodulation play a role in the interactions between the CPG neurons [34, 43, 1]. Whether intrinsic neuromodulation is ubiquitous in CPG circuits has not been determined, as it has not been extensively studied. Yet some think that it may be as common as extrinsic neuromodulation [34].

Neuromodulation can be a presynaptic or postsynaptic mechanism, and can exist in the form of facilitation or inhibition. In this study, we are investigating a form of presynaptic neuromodulation induced by 5-HT, and hence we will focus our discussion on presynaptic facilitation and inhibition. Short-term presynaptic facilitation induced by 5-HT has been thoroughly studied in *Aplysia*. The two principal pathways that

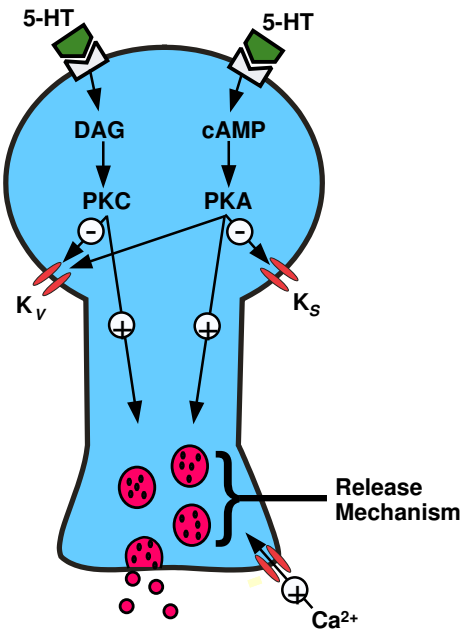

Figure 1: *Mechanism for pre-synaptic facilitation.* Two second messenger cascades lead to the closing of the two potassium channels (S-type and V-type) and to the enhancement of neurotransmitter release by direct action onto the release machinery. Adapted from [5]

lead to facilitation are (a) indirect action onto potassium channels which leads to spike broadening and greater neurotransmitter release, and (b) second messenger cascade directly affecting neurotransmitter release machinery independent of spike-duration and enhancing neurotransmitter release. [5]

In *Aplysia*, it was found that a potassium channel with weak voltage-dependence (named the S-type potassium channel or I_{KS}) and a slow voltage-dependent transient current (I_{KV}) are modulated by 5-HT, adenosine cyclic monophosphate (cAMP) and protein kinase A (PKA), as well as diacylglycerol (DAG) and protein kinase C (PKC).

The second messenger cascades that are believed to lead to this decrease in total conductance are represented in figure 1. For the PKA-mediated cascade, 5-HT binds to a serotonin receptor, increasing the rate of synthesis of cAMP from ATP. As a result, cAMP acts on PKA to release the active catalytic subunits, which lead to phosphorylation and closing of the potassium channels. For the PKC-mediated

cascade, 5-HT is thought to lead to the formation of diacylglycerol and the activation of the PKC, also leading to phosphorylation of the potassium channels (see references in Baxter et al 1999). Reducing the conductance of a potassium current leads to spike broadening as the conductance of potassium currents is responsible for determining the steepness of the repolarization phase of the action potential. Spike broadening in turn leads to an increase in Ca^{2+} current, resulting in enhanced neurotransmitter release.

The spike-duration-independent pathway for facilitation uses the same second messenger cascades described above to act directly on the neurotransmitter release machinery. This research was prompted by the results from previous modeling studies, which showed that spike broadening alone was not sufficient to account for the amount of facilitation observed [5]. The details of this second process leading to facilitation are not known, though one possibility is that the protein kinases act on neurotransmitter vesicle mobilization or on exocytosis. It has also been postulated that PKA and PKC enhance Ca^{2+} channel currents near the active zones, leading to increased neurotransmitter release [35].

Mechanisms similar to the ones described above could lead to presynaptic depression (i.e. second messenger cascades leading to spike narrowing and direct decrease in neurotransmitter release). Though there have been studies describing serotonin-mediated spike-narrowing [27, 44], the mechanisms leading to spike narrowing mediated by 5-HT and A-current modulation have not been described in the literature. It has been suggested that 5-HT released heterosynaptically binds to 5-HT receptors, enhancing cAMP synthesis, activating protein kinases, phosphorylating potassium channels, which leads to an increase in the conductance of those channels (see figure 1).

2.2 Spike-Timing Dependent Neuromodulation

A recently described form of heterosynaptic neuromodulation, called spike-timing dependent neuromodulation (STDN), varies synaptic strength depending on the timing of activity of the neuromodulatory neuron. STDN was first observed in the escape swim CPG of the mollusk *Tritonia diomedea*, and is believed to play a role in pattern generation, though its significance has not yet been determined [43].

Sakurai and Katz (2003) found that *Tritonia*'s dorsal swim interneuron (DSI) modulates the amplitude of the synaptic output of the ventral swim interneuron B (VSI-B) in a timing-dependent manner [43]. When VSI-B is stimulated to fire within 10 seconds after a DSI spike train, VSI-B's synaptic output to the ventral flexion neuron (VFN) is potentiated; when VSI-B is stimulated to fire 20-120 seconds after a DSI spike train, VSI-B's synaptic output to VFN is depressed. A graph of EPSP amplitude in DFN evoked by VSI-B versus time between the DSI spike train and a VSI action potential is shown in figure 2. This plot can be fit with a double exponential function, which implies the existence of two independent modulatory mechanisms, a rapid enhancement (with a time constant of 19 sec) and a slower depression (with a time constant of 69 sec). This is the first study to describe two heterosynaptic modulatory actions acting on the same neuron with different time courses.

Both the facilitation and the depression phase of STDN are believed to be mediated by 5-HT in *Tritonia*'s escape swim CPG. Past studies have shown that DSIs are serotonergic and use serotonin as a neuromodulator [33, 31, 40]. Results from recent experiments conducted by Sakurai and Katz imply that both mechanisms are serotonin-mediated. Bath application of serotonin was shown to block DSI-induced depression and potentiation. As the neurotransmitter perfuses slowly into the ganglia, its concentration increases steadily, and hence potentiation dominates depression. Therefore, the EPSP in VFN is larger than in the baseline experiment (no bath applied serotonin, no DSI activity).

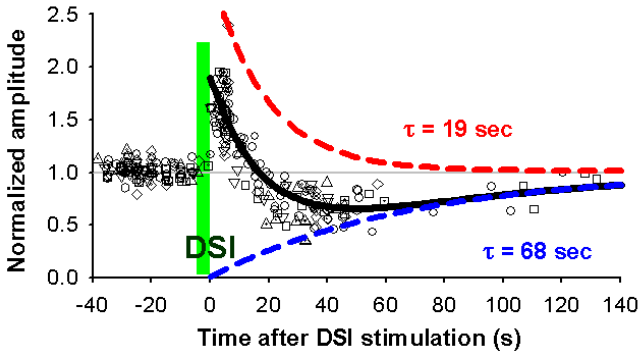

Figure 2: *VSI-B-evoked EPSP amplitude is dependent on previous DSI activity in a biphasic and bidirectional manner.* DSI activity 0-10 seconds before VSI-B spike leads to facilitation in EPSP. DSI activity 20-120 seconds before VSI-B spike leads to depression in EPSP. The green bar in the figure represents a 5 sec DSI stimulation at 5-10 Hz. The data from 5 preparations are shown on the figure. The thick black line represents a double exponential fit with two time constants ($\tau_1 = 19$ sec, $\tau_2 = 68$ sec) From [43]

When DSI stimulation preceded VSI-B firing in bath-applied 5-HT, the potentiation and depression neuromodulatory effects were not observed. This could be because the serotonin released by DSI does not affect the total serotonin concentration, as the serotonin bath concentration is very high ($100\mu M$). Bath application of methysergide, a serotonin receptor antagonist, blocks potentiation or depression in VSI-B-evoked EPSCs. These results also imply that serotonin is responsible for the bidirectional spike-timing dependent modulation, since this behavior is not exhibited when serotonin is not allowed to bind to serotonin receptors on VSI-B. The serotonergic mechanisms of potentiation and depression of the EPSP are not yet known. Physiological evidence has suggested that the depression phase of STDN is mediated by 5-HT enhancing a fast transient outward current, which would lead to spike narrowing, and thus a decrease in neurotransmitter release (see figure 3).

Experiments conducted by Sakurai and Katz show that the A-current channel blocker 4-aminopyridine (4-AP) prevents the serotonin induced depression phase of STDN [42]. These experiments suggest that modulation in A-current is responsible for the spike-timing dependent depression recorded in VFN. 4-AP has also been shown

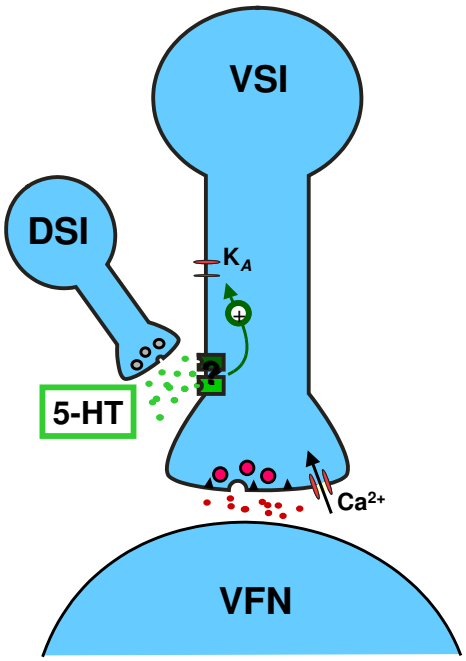

Figure 3: *Hypothesis for depression phase in STDN.* Serotonin from DSI would act on a serotonin receptor, which would act through an unknown second messenger cascade onto the A-current channels. The enhancement of the A-current results in narrowing of spike shape, leading to a synaptic depression.

to increase the width and amplitude of the VSI-B action potential shape (see figure 15). This effect of 4-AP implies that the A-current has a role in determining the shape of the action potential. An enhanced A-current could narrow the spike shape, leading to a weaker synaptic strength. One of the aims of this study is to test the feasibility of this hypothesis using a conductance-based model of the VSI-B.

To investigate the dynamics of STDN experimentally, single VSI-B stimulation was replaced by a spike train of 5 extracellular stimuli, with a frequency of 10 Hz, to simulate a swim pattern. When DSI fired 35 seconds before the spike train was initiated, the depression in VFN due to DSI was only observed in the first EPSCs, the later EPSCs showed little to no depression (see figure 4) [43]. This implies that the mechanism for depression gradually switches off or weakens its hyperpolarizing effect with the progression of the spike train.

The A-current in *Tritonia* has been described as slowly inactivating, with a time

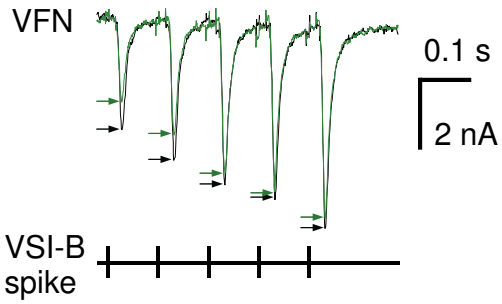

Figure 4: *Dynamics of depression phase of STDN.* Plots of a spike train of five VSI-B evoked EPSPs measured in VFN with no DSI activity (grey arrows) and DSI activity 35 seconds preceding the VSI-B spike train (black arrows). DSI's modulatory action (presynaptic depression) is reduced at the end of the spike-train. From [43]

constant of 235-760 ms [7, 14]. If the A-current enhancement were to mediate the depression phase of STDN, the A-current would inactivate during the time course of the spike train evoked EPSCs in VFN, leading to a decrease in depression, as has been observed and described in reference [43]. This is an additional reason to believe that the A-current has a role in STDN. The feasibility of this hypothesis will also be tested with simulations of a VSI-B spike train using the model, and studying how much the A-current inactivates during the progression of the spike train.

The cellular mechanisms underlying the proposed hypothesis have not been confirmed empirically. Previously studied neuromodulatory mechanisms in *Aplysia* would suggest that a second messenger cascade is likely to be involved. A possible mechanism for depression is shown in figure 3, and can be described as:

1. The DSI burst leads to 5-HT release onto the VSI-B.

2. 5-HT binds to 5-HT receptors on VSI-B.

3. This enables synthesis of a second messenger, which acts directly or indirectly on A-current channels. This could involve, for example, an activation of a protein kinase that leads to phosphorylation of the channel or direct action of a G-protein on the channel.

4. This enhances the A-current conductance, leading to spike narrowing.

5. Less neurotransmitter is released, thus reducing synaptic strength of VSI-B.

Experimental results to test this possible mechanism of depression have not yet been published, though preliminary experiments by Dr. Sakurai have thus far confirmed this hypothesis. Although 5-HT most probably acts via other mechanisms, one of the aims of this modeling study is to verify whether spike narrowing alone is sufficient to account for the depression observed during STDN.

2.3 Tritonia Escape Swim

To better appreciate the specific context of STDN in *Tritonia*, a description of the animal's escape swim behavior and its CPG controlling swimming will be presented in this section.

2.3.1 The Behavior

Tritonia diomedea, a nudibranch mollusk, displays an escape swimming behavior . This behavior was first characterized in *Tritonia* by Willows (1967) [47]. Escape swimming is elicited by the rare contact with a predator (such as the starfish), or when in proximity with a high concentration of salts (used to trigger the behavior in an experimental setting). Before the onset of escape swimming, the animal withdraws all of its external organs: the oral veil, rhinophores, and branchial tufts. This is followed by an elongation of the animal, in preparation for swimming. The escape swimming is initiated by a brisk ventral flexion, to propel the animal off the surface of the ocean floor, and continues with a series of 2-20 alternating dorsal and ventral flexions. The escape swim ends with a termination stage, which includes weak dorsal flexions followed by the animal's normal crawling behavior on the seabed [47, 48, 38, 13, 15, 14]. The behavior is not intended to be a coordinated swim, where direction is important, but instead simply drives the animal out of danger, by placing it far

enough from the ocean floor to be displaced by ocean currents [15]. This behavior has been studied for over 30 years because of its CPG circuit, whose neurons and synaptic connections have been identified and characterized. It is possible to investigate the role of each neuron in the initiation and maintenance of the escape motor pattern because of the low number of escape swim CPG neurons.

2.3.2 The Central Pattern Generator Circuit

The escape swim has been linked to the activity of an identified group of neurons, forming a CPG circuit. The CPG controlling the escape swim is found in the cerebral-pleural-pedal ganglion complex [47]. It is comprised of three types of neurons: the cerebral interneuron two (C2), the ventral swim interneuron (VSI), and the dorsal swim interneuron (DSI); there are 2 C2s, 4 DSIs, and 2 VSI-B that comprise the the neural CPG circuit [13]. Two groups of VSIs have been identified, VSI-A and VSI-B, but VSI-A does not play a defining role in the pattern generation. Each type of neuron (except VSI-A) is a necessary component of the CPG, but none of the cells are sufficient to produce the pattern when isolated, which demonstrates the critical role of the synaptic connections [15].

As each neuron type (eg. any one DSI) has the same synaptic inputs and modulatory actions, identifying the individual neuron of a given type is not necessary when discussing the CPG. Figure 5 shows a graphical representation of the neurons in the CPG and their synaptic connections. The interneurons connect synaptically to other neurons or to themselves, and can form inhibitory connections, excitatory connections, or both (transiently). VSI monosynaptically inhibits DSI and C2; DSI inhibits VSI and excites C2; C2 has a delayed excitatory connection to VSI-B, and has a multi-component synapse onto DSI (C2 initially excites then inhibits DSI) [13, 14, 43].

The cellular properties of the neurons will be introduced because they are as

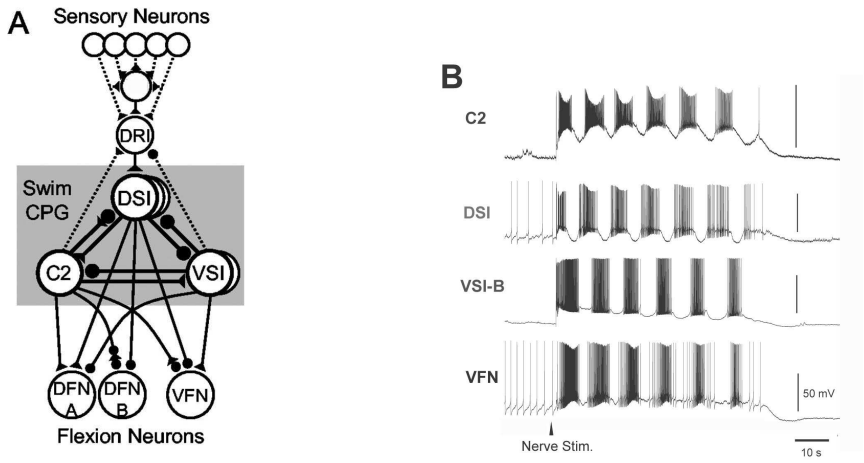

Figure 5: *The escape swim CPG and swim motor pattern. A,* A graphical representation of the escape swim CPG in *Tritonia diomedea* and its input and output neurons. The triangular synapses represent excitatory connections and the circular synapses represent inhibitory connections. *B,* An example of the swim motor pattern. The swim was initiated by stimulating a nerve in the pedal ganglion, and the intracellular recordings of C2, DSI, VSI-B, and VFN activity were taken simultaneously. From [43]

crucial to pattern generation as the synaptic connections between neurons. The DSI have a low threshold, and fire action potentials spontaneously at rest. On the other hand, C2 and VSI-B have a threshold 10-15 mV above rest potential, and hence must be depolarized to fire. An A-current has been identified in all interneurons, but as the resting potential of VSI-B is lower than the other interneurons, the A-current is not completely inactivated at rest, which results in a delay between initial depolarization of the neuron and the onset of the first action potential of the VSI-B [13, 14].

STDN is hypothesized to have a role in pattern generation. Stimulating a DSI and VSI-B burst pattern similar to a swim and measuring EPSC amplitude enabled some analysis of how STDN affects the pattern generation [43]. The burst duration of VSI-B is under 10 sec, and is preceded by a DSI burst, so the synaptic strength is enhanced during the VSI-B burst. More experimental and modeling studies must be conducted to fully understand STDN's role in the escape swim pattern generation.

CHAPTER III

APPROACH AND METHODS

For this thesis, we have constructed a model of the VSI-B neuron from the escape swim CPG in *Tritonia diomedea*. This model will be used to test whether A-current modulation is sufficient to account for the the depression phase of STDN. This will be done by studying how increasing A-current conductance affects spike shape, thus determining the magnitude of VSI-B synaptic release onto VFN. Such results would provide evidence of feasibility of the hypothesis that an increase in A-current conductance (mediated by serotonin) is responsible for a decrease in synaptic activity in VSI-B, leading to a depressed EPSC in VFN. This model will also allow us to study the A-current transient during an escape swim. By simulating a swim VSI-B burst, we can follow the A-current amplitude during the different stages of the swim burst.

The approach to modeling the VSI-B consists of using a Hodgkin-Huxley-style gating model to incorporate the principal ion channels present in the VSI-B [25]. By adjusting the conductances and gating properties of each channel, a physiologically accurate model of the electrical activity across the membrane can be constructed. Though the initial phase assumes an isopotential single compartment, we want to have the flexibility of modifying the morphology to a more complex (and accurate) one. For this reason, the NEURON simulation environment was chosen to construct this model. NEURON is a software simulator designed for implementation of neural models based on empirical data, see references [22, 23, 24]. NEURON enables the creation of multi-compartment models, incorporating cable theory and differential equation solving to describe electrical activity at different points on the neuron. NEURON was also chosen for its ease of creating neuronal networks (expendability of my model), and

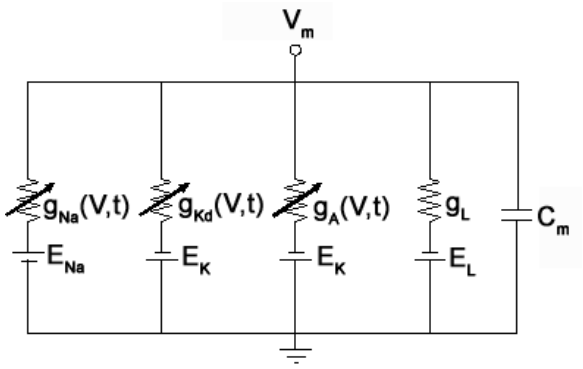

Figure 6: *The VSI-B circuit model.* The membrane capacitance is represented by the capacitor (C_m); each ion channel is represented by a battery(E_{rev} - its reversal potential) and a conductance (g_{ion} - the channel conductance). This circuit model is based on the Hodgkin and Huxley giant squid axon model [25].

for its portability of simulations.

3.1 Hodgkin-Huxley Style Modeling

Hodgkin and Huxley proposed a breakthrough model of a giant squid axon neuron in 1952, used to describe the non-linear behavior of ionic currents in neurons, and their effect on the total membrane current and voltage [25]. The neuron was represented by an electrical circuit, similar to the one shown in figure 6. In this parallel conductance model, the capacitor represents the membrane capacitance; each ion channel is modeled as a battery (its reversal potential) in series with a variable conductance (proportional to number of channels open). Using Kirchoff's voltage law, the following equation can be extracted from the circuit assuming no current is injected into the system:

$$-C_m \frac{dV}{dt} = \sum_{j=ion} I_j \tag{1}$$

where C_m is membrane capacitance, V is membrane across voltage, I_j is the current across a specific ion channel. Since the ion channel current is calculated from Ohm's law across the conductance, equation 1 can be rewritten as:

$$-C_m \frac{dV}{dt} = \sum_{j=ion} g_j(V - E_j) \tag{2}$$

where g_j is the voltage and time dependent conductance of ion channel j, and E_j is its reversal potential. The function g_j can be described by a maximal conductance multiplied by a comprehensive gating variable that varies from zero when the channel is completely closed to one when the channel is maximally open. The comprehensive gating variable is the fraction of any one type of ion channel that is open, and is represented by the product of a power of the activation variables (n or m) and inactivation variables (h). For example, the conductance function for the fast sodium ion channel can hence be expressed as:

$$g_{Na} = \overline{g}_{Na} m^3 h \tag{3}$$

where $\overline{g}_{Na}$ is the maximum conductance of sodium, the activation variable (m) is raised to the third power, and the inactivation variable (h) to the first. The gating variables can be described by a set of ordinary differential equations related to the steady state probabilities of the channel being in the open state (as $t \to \infty$) and the time constant (which is voltage dependent). Again taking for example the sodium channel, the activation variable kinetics can be described as:

$$\frac{dm}{dt} = \frac{m_\infty(V) - m}{\tau_m(V)} \tag{4}$$

where m_∞ is the (voltage-dependent) steady state activation function, and τ_m is the (voltage-dependent) time constant function for activation. Each of these can be modeled as with a sigmoidal function, which depends on the half-activation voltage (voltage at which the function is half its maximum value) and half-activation slope (slope at the half activation point). Generic versions of the functions m_∞ and τ_m are shown in figure 7 and described as:

$$m_\infty = \frac{1}{1 + e^{\frac{V - V_{half}}{S_{half}}}} \tag{5}$$

$$\tau_m = \tau_{min} + (\tau_{max} - \tau_{min}) \frac{1}{1 + e^{\frac{V - \tau_{half}}{S_{half}}}} \tag{6}$$

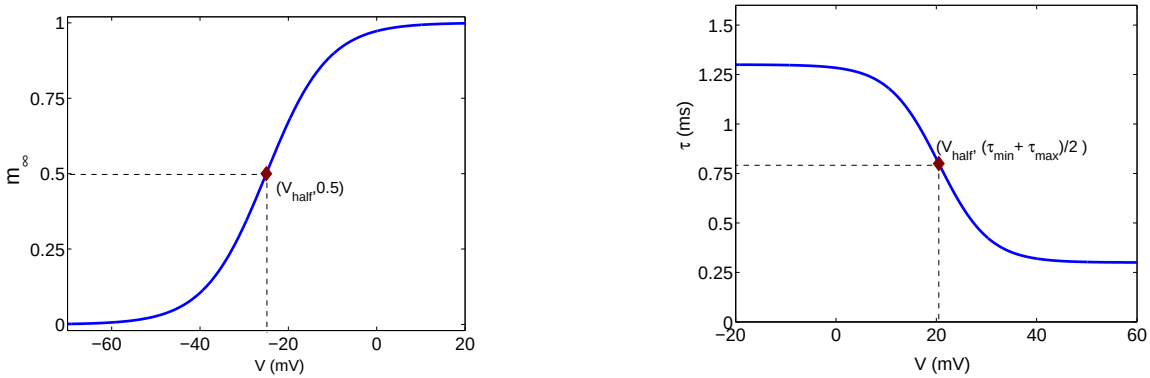

Figure 7: *Fictitious activation and inactivation variables. A,* A plot of a fictitious steady state activation variable (m_∞), where $V_{half} = -25mV$ and $S_{half} = -7$; *A,* A plot of a fictitious time constant function, where $\tau_{half} = 20.5mV$, $S_{half} = 5$, $\tau_{min} = 0.3ms$, and $\tau_{max} = 1.3ms$

where V_{half} is the half-activation voltage, S_{half} is the half-activation slope, τ_{half} is the half activation time constant value, τ_{min} is the minimum time constant, and τ_{max} is the maximum time constant. (Note that the values for S_{half} are often different for the steady state activation and time constant.) Though time constants are often described as bell shaped curves, as in the original Hodgkin-Huxley squid axon model, the physiologically relevant portion of the bell shaped curve (V = -70 to +50 mV) can be fitted with a sigmoidal curve, and hence was chosen for simplification of the model due to a lower number of parameters.

Giant Squid Axon Model. The first Hodgkin-Huxley model was based on the giant squid axon, and comprised of three ion channel currents: a fast sodium channel, with an activation and an inactivation variable, a delayed rectifier potassium channel, with only an activation variable, and a leak channel, with a constant conductance obeying Ohm's law. As its name suggests, the fast sodium current is a fast inward current which causes a rapid depolarization of the membrane. The delayed rectifier is a potassium channel causes an outward current that counters the sodium current after a slight delay from onset of the depolarization, and de-activates as the membrane voltage is brought back towards rest. These three channels are sufficient

to simulate electrical activity, producing action potentials when a super-threshold stimulus current is passed through the membrane (by addition of a I_{stim} to the right side of equation 1).

Channels in VSI-B. The three ion channel currents modeled in the original giant squid axon model are also present in VSI-B (as with most invertebrate neurons), though the dynamics are not quite the same. Voltage clamp traces for the delayed rectifier potassium and the fast sodium currents are not available, as pharmacological ion channel blockers such as tetraethylammonium (TEA), a delayed rectifier potassium channel blocker, or tetrodotoxin (TTX), a fast sodium blocker, partially block these currents in *Tritonia*. Therefore, we cannot develop a model of these currents from experimental data, and must rely on models and data from other invertebrate animals.

The A-current is also known to exist in VSI-B. The A-current, first described by Connor and Stevens (1971), is de-inactivated by a hyperpolarizing pre-pulse, and is fully activated by a depolarizing pulse [8]. The A-current in VSI-B has been quantified and modeled in previous studies [14, 16], though it is believed to be inaccurate. Preliminary electrophysiology experiments have been the basis for a renewed model of A-current (see section 4.3).

CHAPTER IV

RESULTS

4.1 Modeling VSI-B using Getting's A-current model

Initially, a model for VSI-B was developed by building upon on a previous model for the A-current in *Tritonia*, from reference [16]. Getting constructed a non-physiologically based model of the escape swim CPG circuit using integrate-and-fire neuronal models, and had included an A-current that he had based on his voltage clamp data published by Getting (1983) [14]. Since the A-current was based on electrophysiological data, it was used "as is" in the first version of the VSI-B model in this study, with the exception of the inactivation curve. The A-current was described by Getting as:

$$I_A = \overline{g}_A \cdot m \cdot h \cdot (V - E_K) \tag{7}$$

The parameters for the A-current are shown in the Appendix.

To model VSI-B, the ionic currents in VSI-B must be identified, and the kinetics of each channel must be known. As the kinetics for the three channels in the original squid axon model are similar to VSI-B, this model was used as a beginning point. The activation and inactivation curves for these channels were not changed much, though the time constants were scaled up as the action potential width is larger in VSI-B neurons than in the squid axon, and hence the time constants are larger. As the original Hodgkin-Huxley equations were expressed in α, β form (in terms of forward and reverse rates), activation curves in sigmoidal form (as the ones presented earlier in chapter 3) were extracted.

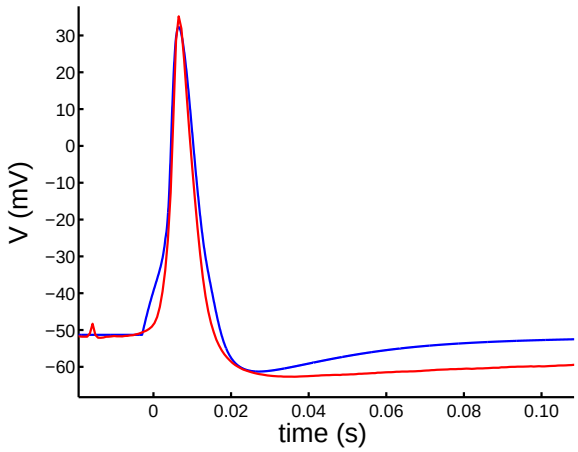

Figure 8: *Action potential shape for model and experiments.* The action potential from experimental recordings (red) was stimulated extracellularly with a short-duration high voltage in a saline solution, and averaged over five trials ($n = 5$). The simulated action potential (blue) was evoked using an intracellular stimulus current of 8 nA for 3 μs.

Single spike activity – action potential shape. To model the VSI-B, the first step was to reproduce the action potential shape. Electrophysiology data was obtained from Dr. Sakurai, who stimulated the VSI-B with a brief, strong extracellular stimulus in the pedal nerve 6, therefore evoking a single back-propagated action potential, and recorded the transient voltage trace in the soma. The initial goal was to match the model to single action potential data. To widen the pulse, the time constants were first multiplied by a factor of about ten and then adjusted along with the conductance of each channel so that the fast sodium channel turned on first and the delayed rectifier reached its maximum conductance shortly after the action potential reaches its maximum voltage value. The slopes of the rising and falling edges of the action potential could also be controlled by adjusting the time constants. To increase the maximum amplitude of the action potential, the sodium maximal conductance was increased, hence increasing the initial inward current. To vary the maximum hyperpolarization of the action potential, the potassium delayed rectifier maximal conductance was adjusted. The action potential trace was produced by injecting a large step current of amplitude 8 nA, and recording the transient simulation. There is

no delay because of the large current injected for 3 μs, which counters the inhibitory effect of the A-current.

The calcium and calcium-activated potassium currents were not included in the model. The calcium-activated potassium current current was initially added to model the action potential's slowly recovering post-hyperpolarization hump, which was not thought to be due to the delayed rectifier current. Though not physiologically accurate (since no calcium current has been modeled), the modeled outward current was triggered by spiking (when calcium influx is large and fast) and decayed slowly. At the expense of spike shape not reproducing the post-repolarization hump, the calcium-activated potassium current was removed from the model to keep the model as simple as possible. The calcium current is not believed to have a significant role in the electric activity of the VSI-B membrane, and thus was left out of the model.

Tonic firing patterns and delay due to A-current. The next step in building the initial VSI-B model was to reproduce the tonic firing patterns of the neuron. Ideally, the simulation's spike frequency response to a sustained stimulus would be fully reproduced. The frequency can be increased by enhancing the conductance of the sodium current, and decreased by enhancing the conductance of the delayed rectifier current. A plot of maximum frequency versus injected stimulus current magnitude was published in reference [14], and reproduced with the model (see figure 9).

A principal characteristic of the VSI-B is the delay between the onset of the current stimulus and the onset of action potential firing. As mentioned earlier, the A-current is responsible for this delay. Initially, Getting's A-current model was used in the VSI-B model, but it was observed through simulations that the A-current did not turn on when a stimulus was applied. This is due to the shape of the inactivation curve in Getting's model, where at rest the VSI-B is almost completely inactivated. Hence, even when the neuron activates fully due to depolarization, the A-current

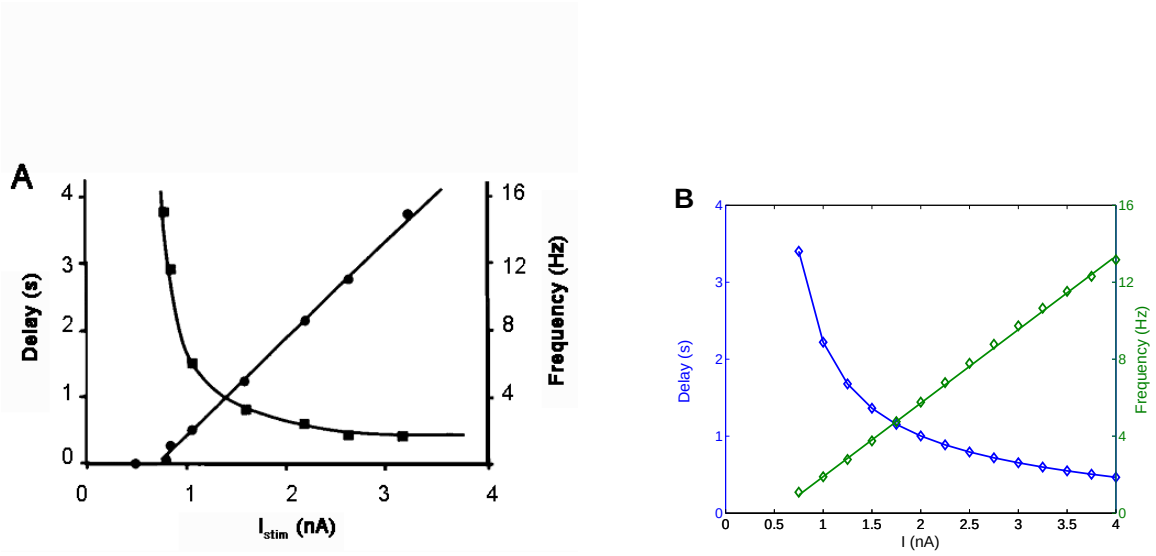

Figure 9: *VSI-B firing properties.* A plot of the frequency versus stimulus current and delay versus stimulus current from (A) experiments in normal saline (from [16]) and (B) from the model.

is already mostly inactivated, and so the current was never turned on. To correct this, we shifted the inactivation curve to the right, so that at rest, the current was only partially inactivated. This partial inactivation allowed the channel to open with the fast activation, before closing due to the slow inactivation. A hyperpolarizing pre-pulse would de-inactivate the neuron further, leading to an enhanced A-current during depolarization.

Changing the A-current dynamics, and adjusting its conductance, allowed the neuron to exhibit the delayed response to a depolarizing stimulus. The magnitude of the delay was adjusted by increasing or decreasing the A-current maximum conductance, which increased or decreased the delay, respectively. A plot of delay versus injected stimulus current magnitude was published in reference [14], and was reproduced with the current model (see figure 9).

Diameter and resting conductance of VSI-B. The diameter of the soma of VSI-B ranges from 40 to 60 μm [14]. The diameter of the single compartment neuron was modeled as 300 μm for two reasons: (a) to account for membrane invagination

[19, 41]; (b) to account for the initial segment of the axon which was also clamped in addition to the soma. The value for resting conductance in VSI-B was calculated from experiments. A short weak hyperpolarizing pulse was injected in the VSI-B soma, and its voltage response was recorded. We can then calculate resistance using Ohm's law ($g = \Delta I/\Delta V$), where ΔV is maximum voltage difference. A hyperpolarizing input current of 0.25 nA for a period of 2 seconds resulted in an average response of 3.5 mV and a resting conductance of 71.4 nS. To calculate the resting conductance of the model, we must first find the steady state of the gating variables at rest. We can then find the conductance of each current by multiplying the gating variables of the current by the maximal conductance. The total resting conductance is:

$$g_{rest} = \overline{g}_A \cdot h_A \cdot m_A + \overline{g}_{Kd} \cdot {n_{Kd}}^4 + \overline{g}_{Na} \cdot {m_{Na}}^3 \cdot h_{Na} + \overline{g}_{leak} \tag{8}$$

The rest conductance using this model is 4.45 μS, which is not within physiological range.

Limitations and Revisions to Getting's A-current model. After completion of a VSI-B model using Getting's modified A-current model, we decided to model our own A-current, as the voltage clamp data of the A-current that Dr. Sakurai collected showed a more complex A-current dynamics not displayed in Getting's A-current model. For example, the time constants modeled by Getting are constant and therefore voltage independent, which is not the case with Sakurai's data. To calculate the time constants, Getting fitted one voltage clamp current trace with a single exponential. As the time constants are voltage dependent, Getting would have needed to fit each voltage clamp current trace. It was also observed that Sakurai's voltage clamp current traces could not be fit with a single exponential, another indication that Getting's model was not accurate. In addition, the voltage clamp traces presented by Getting (1983) [14] are suspect, as there seem to be spiking activity during the voltage clamp, indicative of poor space clamp. The experiments conducted by Dr.

Sakurai were performed in high divalent cation saline solution, and the model needed to take into account these conditions. Taking these observations into consideration, we decided to develop a revised model of the A-current from Sakurai's voltage clamp data.

4.2 Fitting A-current voltage clamp data

A-current voltage clamp data was initially calculated by subtracting the current recorded in the presence of 4-AP from control current. As 4-AP blocks the A-current, the difference of the two currents is mostly due to the A-current (or the 4-AP-sensitive current). Even though other currents may be partially blocked, we are modeling the 4-AP sensitive current since it is 4-AP which blocks the depression effect in STDN. To activate the A-current, Sakurai used an activation voltage clamp protocol, where the voltage is stepped from a low value such as -90 mV (where all channels are assumed to be completely de-activated) to a series of holding voltages (V_{hold}), and measured the resulting current (see figure 12). Assuming the leak current is equivalent in both control and 4-AP, the leak current would be subtracted away. Yet it was noted that one of the side effects of 4-AP is a increase in leak current, in which case the currents need to be leak-subtracted before subtraction. As the leak conductance is constant (and voltage-independent), the procedure to subtract leak from current traces consists of subtracting a multiple of a current trace where the leak conductance is the sole contributor from a current trace where there is both leak and A-current.

In order to find an equation to which we can fit the voltage clamp traces, we must first develop the equations describing the transients of the activation and inactivation gating variables. We start with the differential equations describing the activation gating variable:

$$\frac{dm}{dt} = \frac{m_\infty(V) - m}{\tau_m(V)} \tag{9}$$

Since voltage does not vary during voltage clamp protocols ($V = V_{hold}$), the steady

state activation variables and time constants are constant. This enables us to solve the differential equation:

$$\begin{aligned}
\int \frac{dm}{m_\infty(V_{hold}) - m} &= \int \frac{dt}{\tau_m(V_{hold})} \\
\int \frac{dm}{m - m_\infty(V_{hold})} &= -\int \frac{dt}{\tau_m(V_{hold})} \\
\ln(m - m_\infty(V_{hold})) &= -\frac{t}{\tau_m(V_{hold})} + K_* \\
\Longrightarrow \qquad m(t) &= K_m e^{-t/\tau_m(V_{hold})} + m_\infty(V_{hold}) \qquad (10)
\end{aligned}$$

Similarly, the inactivation gating variable is found to be:

$$h(t) = K_h e^{-t/\tau_h(V_{hold})} + h_\infty(V_{hold}) \qquad (11)$$

The initial conditions are $m(0) = 0$ and $h(0) = 1$, since at $V = -90\ mV$ the A-current is not activated and not inactivated. This enables us to find constants K_h and K_m:

$$\begin{aligned}
m(t=0) = K_m + m_\infty(V_{hold}) = 0 \quad &\Rightarrow \quad K_m = -m_\infty(V_{hold}) \\
h(t=0) = K_h + h_\infty(V_{hold}) = 1 \quad &\Rightarrow \quad K_h = 1 - h_\infty(V_{hold})
\end{aligned}$$

This gives the equations for activation and inactivation variables:

$$m(t) = m_\infty(V_{hold}) \left(1 - e^{-t/\tau_m(V_{hold})}\right) \qquad (12)$$

$$h(t) = h_\infty(V_{hold}) + (1 - h_\infty(V_{hold}))\, e^{-t/\tau_h(V_{hold})} \qquad (13)$$

We can now fit voltage clamp traces to:

$$I_A = \overline{g}_A \cdot m(t)^4 \cdot h(t) \cdot (V_{hold} - E_K) \qquad (14)$$

This equation is from [8], where the A-current was first described and characterized.

4.2.1 Compensating voltage clamp current trace for $\frac{dV}{dt} \neq 0$

From initial fits, it could be seen that the voltage clamp current traces could not be fit to a single inactivation gating variable. The initial 100 ms of the current transients

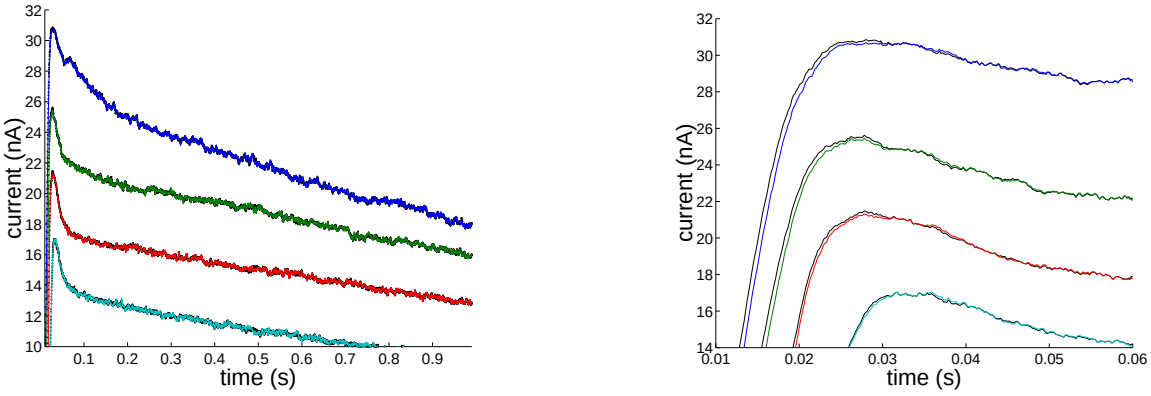

Figure 10: *Compensating for* $\frac{dV}{dt} \neq 0$ *has minimal effect on calculated current. A,* Plots of activation protocol voltage clamp A-current traces (color) and current traces compensated for non-zero $\frac{dV}{dt}$ (black). The corresponding voltage traces are plotted in figure 12 B. *B,* same as A, zoomed in to make difference in plots clear.

display a fast inactivation, followed by a slow inactivation. It was initially thought that the initial fast inactivation might not be physiologically accurate, possibly the result of poor space clamping. As can be seen from voltage clamp voltage data, the initial portion of the voltage trace is not well clamped (see figure 12), especially for high holding voltages. Since the injected current assumes $\frac{dV}{dt} = 0$, we must correct for region where $\frac{dV}{dt} \neq 0$.

Adding a stimulus current (I_{stim}) to equation 2, we have:

$$\begin{aligned} -C_m \frac{dV}{dt} &= \sum_{j=ion} I_j + I_{stim} \\ \implies \sum_{j=ion} I_j &= I_{stim} + C_m \frac{dV}{dt} \end{aligned} \tag{15}$$

For voltage clamp, $\frac{dV}{dt}$ is assumed to be zero, so $\sum_{j=ion} I_j = I_{stim}$. But in the case where $\frac{dV}{dt} \neq 0$ (due to a partial loss of control of space clamp conditions), we must add $C_m \frac{dV}{dt}$ to the voltage clamp current trace. $\frac{dV}{dt}$ was calculated for a the voltage trace with visible non-zero slopes, after low pass-filtering the curves. Using the capacitance of the cell ($C_m = 9$ nF according to [14]), $C_m \frac{dV}{dt}$ was added to the current trace. The comparison between the original and the corrected current trace is shown in figure 10. Since the voltage clamp data displays a fast inactivation after compensating

for $\frac{dV}{dt} \neq 0$, it can be concluded that the non-zero slope of the voltage trace is not responsible for the initial fast inactivation in the voltage clamp current trace of the A-current.

4.2.2 Fitting procedure

As with the A-current in VSI-B, two components of inactivation have been described and modeled in the A-current of another invertebrate species [28, 3]. The next step was to find the appropriate form for the A-current, which was known to be a sum of two inactivation variables. The general form of the equation is:

$$I_A(t) = K_1 \cdot m^4(t) \cdot h_1(t)(V_{hold} - E_K) + K_2 \cdot m^4(t) \cdot h_2(t)(V_{hold} - E_K) \qquad (16)$$

where $m(t)$ is the activation variable in the form of equation 12. $h_1(t)$ is the fast inactivation state variable and $h_2(t)$ is the slow inactivation state variable; both are in the form of equation 13. Initially, it was assumed that the steady state inactivation variables were non-zero for all holding voltages. This results in eight parameters which need to be fit to each voltage trace ($m_\infty(V_{hold})$, $h_{1\infty}(V_{hold})$), $h_{2\infty}(V_{hold})$, $\tau_m(V_{hold})$, $\tau_{h1}(V_{hold})$, $\tau_{h2}(V_{hold})$, K_1, K_2). MATLAB's curve-fitting toolbox was used to fit the current traces. The software was able to fit each of the current traces ($r > 0.95$), but the parameter values extracted for different V_{hold} varied over a large range, indicating that the fitting problem was very under-constrained.

We made several attempts to add constraints in order to extract sensible parameters from the fits. The first was to use the activation and inactivation curves from the activation and inactivation voltage-clamp protocol (respectively) to give values for $m_\infty(V_{hold})$, $h1_\infty(V_{hold})$, and $h2_\infty(V_{hold})$. The activation curve is extracted by measuring the peaks of voltage-clamp trace of the activation protocol for each V_{hold}. This assumes that the at the time of the peak, the level of inactivation has not yet changed because of the slower time constant of inactivation. But in this case, there is a fast component of A-current inactivation, and hence this assumption is not valid.

Therefore we cannot use the extracted parameters from these fits.

We also tried to determine values to $m_\infty(V_{hold})$, $h1_\infty(V_{hold})$, and $h2_\infty(V_{hold})$ by using Getting's A-current activation and inactivation curves. The problem with this approach is that the curves were extracted from experiments in normal saline solution. We are modeling cells in a high-divalent solution, which changes the properties of the activation curves by shifting them to the right (see section 4.3.1).

The problem of under-constraining was solved when further voltage clamp experiments revealed that the A-current fully inactivated after about four seconds. This could not be observed from the earlier voltage clamp data used to extract parameters as it had a duration of one second only. The equation for the transient $h(t)$ could be simplified from equation 13, as $h_\infty(V_{hold}) = 0$:

$$\begin{aligned} h(t) &= h_\infty(V_{hold}) + (1 - h_\infty(V_{hold}))\, e^{-t/\tau_h(V_{hold})} \\ &= e^{-t/\tau_h(V_{hold})} \end{aligned} \tag{17}$$

To further constrain the problem, we manually swept through fixed values for K_1 and K_2. Setting $K_1 = 0.3$ and $K_2 = 0.4$ gave fits for all voltage clamp current traces, with extracted parameters within a tight range, indicating that the problem was well constrained.

Two independent inactivation gating variables implies one of two possible mechanisms. First, the A-current could have two types of ion channels, each with different inactivating mechanisms and similar voltage-sensitivities, leading to one fast and one slow inactivation process. The second possibility is a single type of ion channel with two independent inactivating processes. Further investigation is needed to determine which of the two hypotheses is correct, such as conducting single channel patch clamp experiments. This does not directly affect how the A-current is modeled.

4.3 Extracting parameters from the fits and modeling the 4-AP-sensitive current

After fitting the voltage clamp current traces, parameters for different values of V_{hold} could be extracted. The parameters then needed to be fitted to curves to be used in the 4-AP-sensitive current model. The A-current is activated for voltages greater than approximately -30 mV, as can be seen in figure 12, so the parameters can only be extracted for voltages above -30 mV. For voltages below that, parameter values must be extrapolated by fitting the extrapolated parameters to appropriate equations.

Parameters extracted from the fits have been plotted with equations used to model τ_m, τ_{h1}, τ_{h2}, and m_∞ on figure 11. The parameter m_∞ was fit to sigmoidal form similar to equation 5, τ_{h1} was fit to a sigmoidal form similar to equation 6, and τ_{h2} was fit to a bell shaped curve in the form:

$$\tau_{h2} = \left(\frac{a_1}{1 + e^{\frac{(V - V_{half1})}{S_{half1}}}} + \frac{a_2}{1 + e^{\frac{(V - V_{half2})}{S_{half2}}}} \right)^{-1} \tag{18}$$

The inactivation curve could not be extracted from the voltage clamp data, since we assumed $h_\infty = 0$ for all values of V_{hold} where an A-current was present. Therefore we used an inactivation curve extracted from an inactivation voltage clamp protocol provided by Dr. Sakurai.

The maximal conductance was adjusted to fit the maximum amplitudes in the current traces. The parameters describing the dynamics of the modeled A-current are presented in full in table 1 in the Appendix, and the equation for A-current is:

$$I_A = \left(\overline{g}_{A1} \cdot m^4 \cdot h_1 \cdot + \overline{g}_{A2} \cdot m^4 \cdot h_2 \cdot \right) (V - E_K) \tag{19}$$

where $\overline{g}_{A1} = 0.369$ μS, the maximal conductance of fast-inactivation A-current; $\overline{g}_{A2} = 0.493$ μ S, the maximal conductance of fast-inactivation A-current.

Plots of voltage clamp simulations are shown in figure 12, alongside plots of voltage clamp experiments. The voltage clamp simulation reproduce the essential features of the dynamics of the A-current.

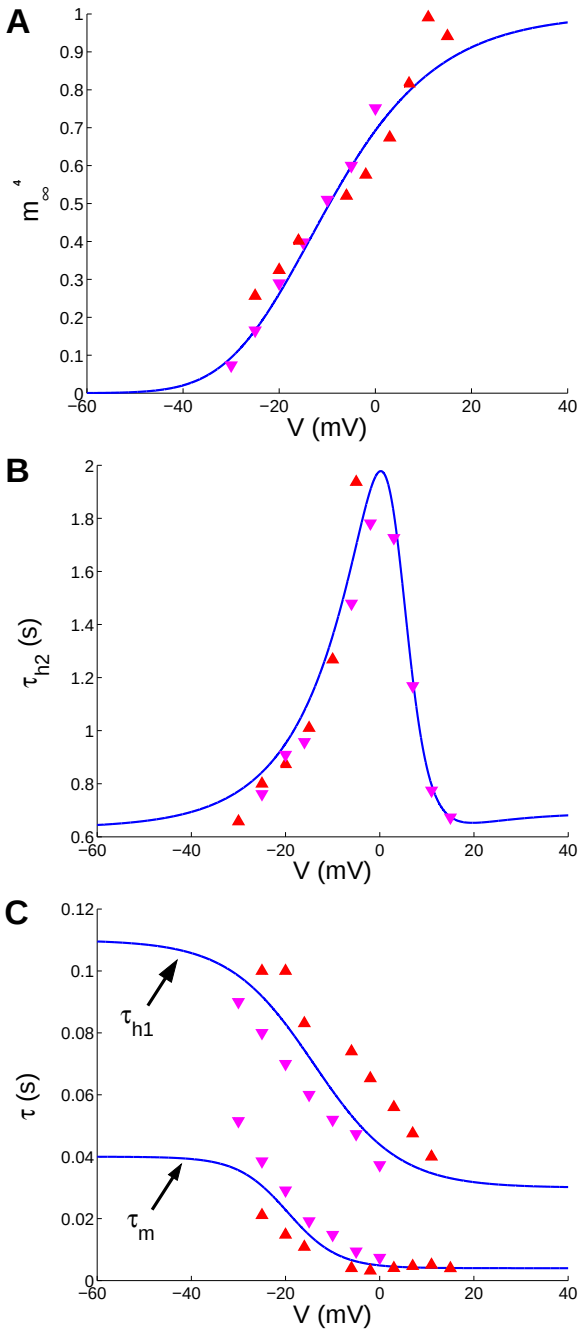

Figure 11: *Extracted parameters fitted to curves used in the new A-current model.* $m_\infty(V_{hold})$, $\tau_m(V_{hold})$, $\tau_{h1}(V_{hold})$, $\tau_{h2}(V_{hold})$ were extracted from voltage clamp fits for -30 mV $\leq V_{hold} \leq$ 15 mV. The red upright triangles and upside down triangles represent two data sets from different experimental preparations. Data is only available for voltage values between -30 mV and +17 mV, as A-current voltage clamp currents are insignificant for V_{hold} below 30 mV and parameters cannot be extracted from those traces. *A*, m_∞ was fit to a sigmoidal function. The activation variable m_∞ is raised to the fourth power in the A-current equation (from [8, 46]). *B*, τ_{h2} was fit to a bell-shaped function. *C*, τ_m, τ_{h1} were both chosen to fit to sigmoidal functions.

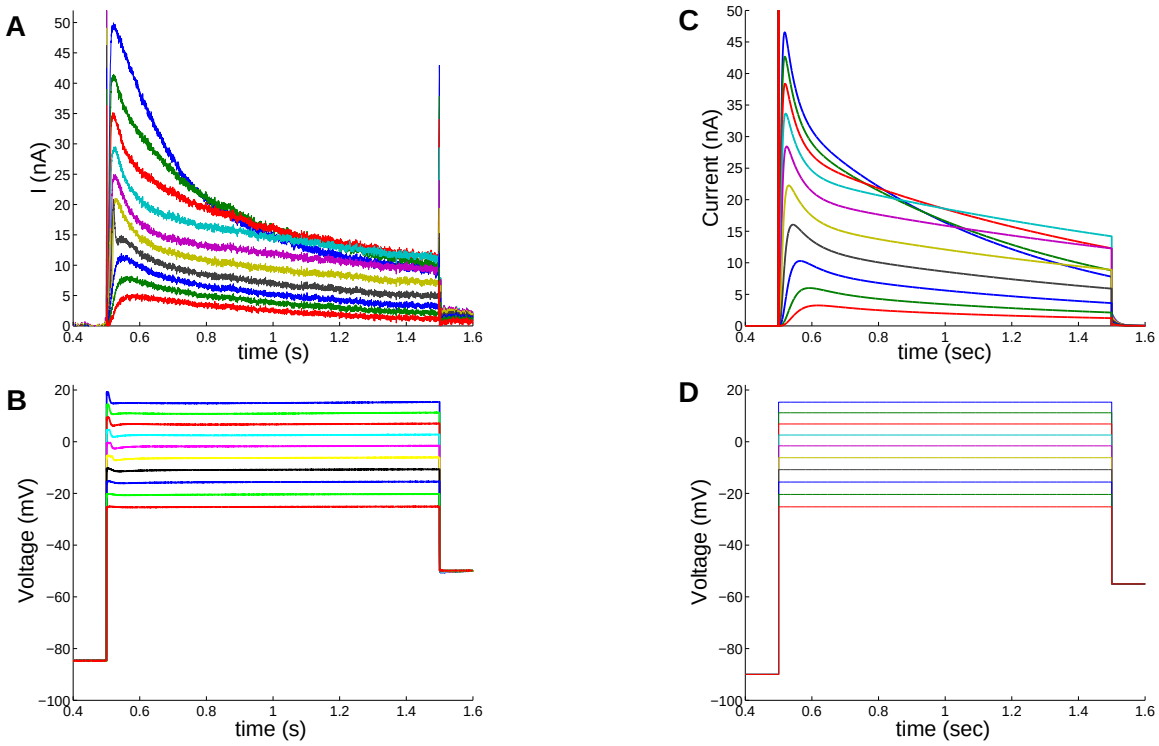

Figure 12: *A-current voltage clamp experiments and simulations. A,* A-current traces for voltage clamp experiments from subtracted data as described in text. *B,* Voltage traces for current response in A. *C,* A-current traces for voltage clamp simulation, where $\overline{g}_{Kd} = 0$, $\overline{g}_{Na} = 0$, and $\overline{g}_{leak} = 0$. *D,* Voltage traces for current response in C.

4.3.1 Comparing the revised A-current model to previously described A-currents

In this section, we will compare the revised A-current model with descriptions of the A-current in *Tritonia diomedea* from previous studies [46, 16]. Though Getting had fully modeled the A-current, Thompson had only characterized it by presenting voltage clamp data, extracted activation and inactivation curves, and time constant curves. Since Thompson had not fit the curves, we fit them to be able to compare them visually with other curves. Getting's data was fit in his model of the A-current, presented in reference [16]. Figure 13A shows A-current activation and inactivation curves from Thompson, Getting, and the revised model. Thompson's and Getting's curves are comparable, but both activation and inactivation curves for the revised model are shifted by about +30 mV (a larger amount of depolarization is needed to open and close the A-current gates).

This shift was initially thought to be an inconsistency with the data from the two published experiments. However, the reason for the shift could be explained by the experimental conditions. The voltage clamp experiments were conducted in a high Ca^{2+} and high Mg^{2+} saline solution, in order to block polysynaptic input. Yet this also has an effect of shifting the activation and inactivation curves [12, 18, 17, 20]. This effect has been attributed to charge shielding, a phenomenon where the divalent cations accumulate on the negatively charged phospholipid group on the cell membrane, causing an ion channel to "see" a higher membrane voltage, as it is located on the membrane [12].

The activation time constant in the revised model was fit to a sigmoidal function, and spans two orders of magnitude. It is shown in figure 13B with data and fits from Thompson and modeled parameters from Getting. Again, a sigmoidal function was chosen to fit Thompson's activation time constant data. The lack of data from Thompson study makes it difficult to know if the fit is accurate outside the voltage

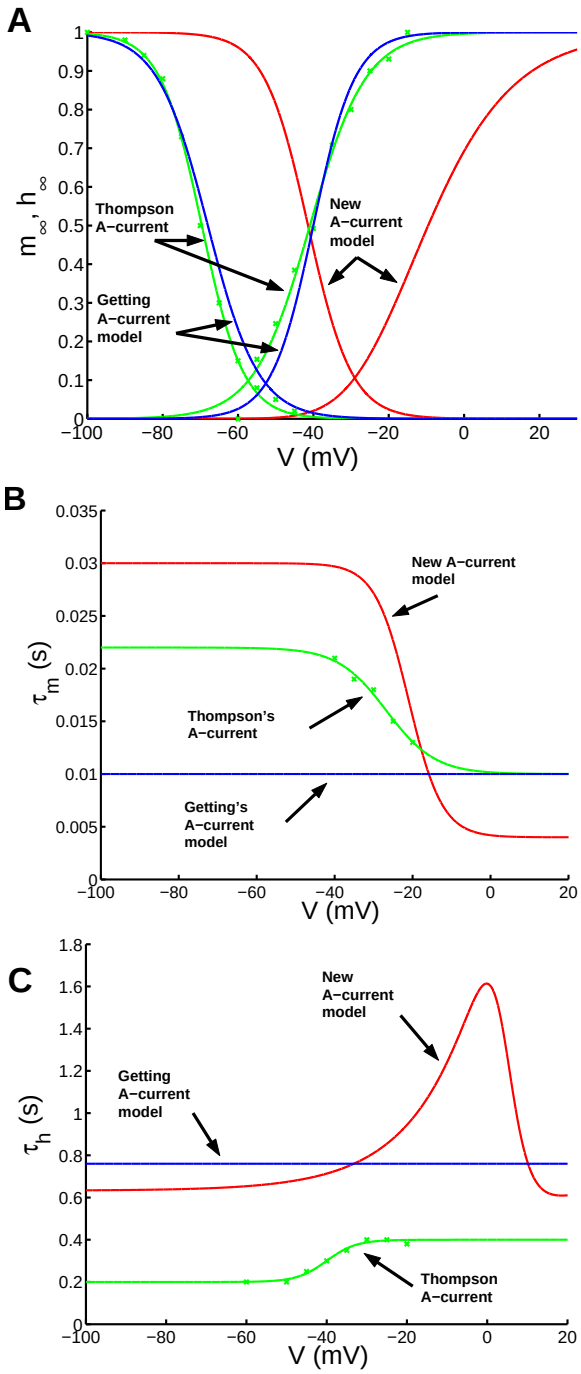

Figure 13: *Comparison of the new A-current model with data and model from Getting and Thompson.* In order to compare the three A-current descriptions, this figure shows the activation and inactivation curves (panel A), the activation time constants (panel B) and the inactivation time constants (panel C). Thompson's data from [46] is shown as green data points. We then fitted curves (in green) to this data for easier comparison.

ranges for which data exists.

The slow inactivation time constant from the revised model (τ_{h2}) is plotted with the inactivation time constants from Thompson and Getting in figure 13C. The revised model is on the same order of magnitude than Getting's voltage-independent time constant, and 3-4 times greater than the fit to Thompson's data. While Thompson's data was chosen to be fitted with a sigmoid, it could have been fit with a bell shaped curve; the main limitation to the Thompson fits is number of data points.

4.4 Modeling VSI-B with the revised A-current model

A model of VSI-B was constructed using the revised A-current model described in the previous section. As with the earlier version of VSI-B (using Getting's A-current model), the dynamics for the fast sodium and delayed rectifier currents were based on the squid axon model, and modified to give an action potential shape similar to collected data. The activation and inactivation curves were shifted to account for the charge shielding effect described in the previous section. The leak reversal potential was set near resting potential, as the other currents are almost completely de-activated at rest (due to the shift in activation curves). As the voltage-dependent currents are almost zero at resting potential, the leak conductance is mostly responsible for the resting input conductance. The leak conductance was set to produce an input conductance of 71.4 nS, matching empirical data.

The maximal conductances for the delayed rectifier and the fast sodium current from reference [46] were calculated and used as a starting point to set the maximal conductances in the model. They were further adjusted to match the features of the tonic firing pattern, such as delay in onset of firing, maximum action potential amplitude, action potential width, and inter-spike interval. A plot of tonic firing in experiment and simulation is shown in figure 14.

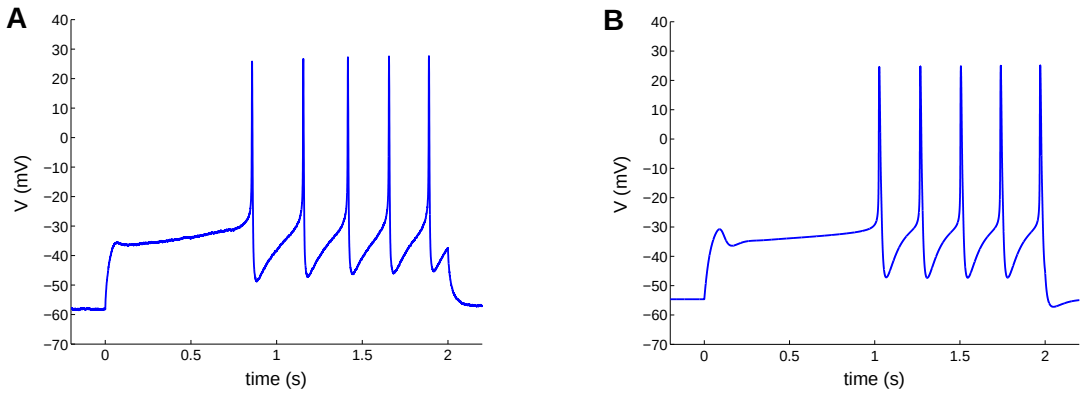

Figure 14: *Tonic firing in experiment and model. A,* A current stimulus of 2 nA was injected intracellularly into VSI-B soma in a high-Ca^{2+} / high Mg^{2+} saline solution. *B,* Simulation results of a prolonged stimulus current step of 2 nA.

After finding a set of parameters that correspond to an accurate tonic firing shape, we swept through 875 sets of neighboring parameters to find other possible sets of parameters which might reveal better fits of the model to tonic firing experiments. The parameters varied are: $\overline{g}_{Na}$, $\overline{g}_{Kd}$, V_{half} for m_∞ for Na, and τ_{max} for K_d. These parameters were chosen as each has a significant effect on specific aspects of the firing pattern. Increasing $\overline{g}_{Na}$ both increases the maximum amplitude of each spike and decreases the delay in offset of firing. The increase of $\overline{g}_{Kd}$ has an opposite effect, increasing the delay and decreasing the minimum voltage of the spike. The fast sodium channel's V_{half} for m_∞ controls the action potential threshold, and the delayed rectifier's τ_{max} increases inter-spike interval (by slowing the post-repolarization de-activation of the potassium channel). The sweep of parameters space permits us to find additional sets of parameters with equivalent A-current dynamics and similar tonic firing patterns.

4.5 Testing a hypothesis for depression in STDN

The conductance-based model for VSI-B enables us to test the hypothesis for the depression phase of STDN. By enhancing $\overline{g}_A$ in the model, we can simulate the proposed actions of 5-HT on VSI-B. The first step is to sweep through $\overline{g}_A$ parameter

space, in order to predict the effect of A-current strength on spike shape. Next, we use experimental results to find a relationship between spike shape and EPSC amplitude. We can then use these results, along with experimental data on spike change, to predict the amount of depression in VSI-B-evoked EPSCs due to change in spike shape alone.

The area of the spike above a threshold of -20 mV was chosen as a metric to compare spike shape. An alternative would be to quantify spike shape using half-amplitude spike width. This alternative measure has its limitations, as it does not take into account the amplitude of the action potential. Two action potentials could have the same spike width, but different spike amplitudes, and hence different amount of neurotransmitter release and evoked EPSC strengths. The area under spike takes into account both spike width and amplitude. The threshold value of -20 mV was chosen as this is the approximate threshold for influx of calcium leading to neurotransmitter release [29]. Therefore, the spike shape above -20 mV is the portion of the action potential relevant for our study.

To observe the effect of changing $\overline{g}_A$ on spike shape, we swept through $\overline{g}_A$ from zero to an enhancement by a factor of two over the nominal value. Keeping all other parameters the same, we swept through $\overline{g}_A$ from zero to an enhancement by a factor of two. Zero conductance mimics the effect of 4-AP, which blocks the A-current channels. The results of the sweep are shown in figure 17, and display an increase in spike area of about 91% when $\overline{g}_A$ is reduced to zero (see figure 15). Experiments in bath-applied 4-AP have led to a spike area increase of 54-240%, displaying a large variability in its effect due to the efficiency of the blockage and the health of the cell during experiments. The model prediction falls within the experimental range, though at the lower end of the range.

5-HT is known to enhance the A-current conductance by 20%, which can also be simulated using the model. Area under the spike reduces by approximately 5% with

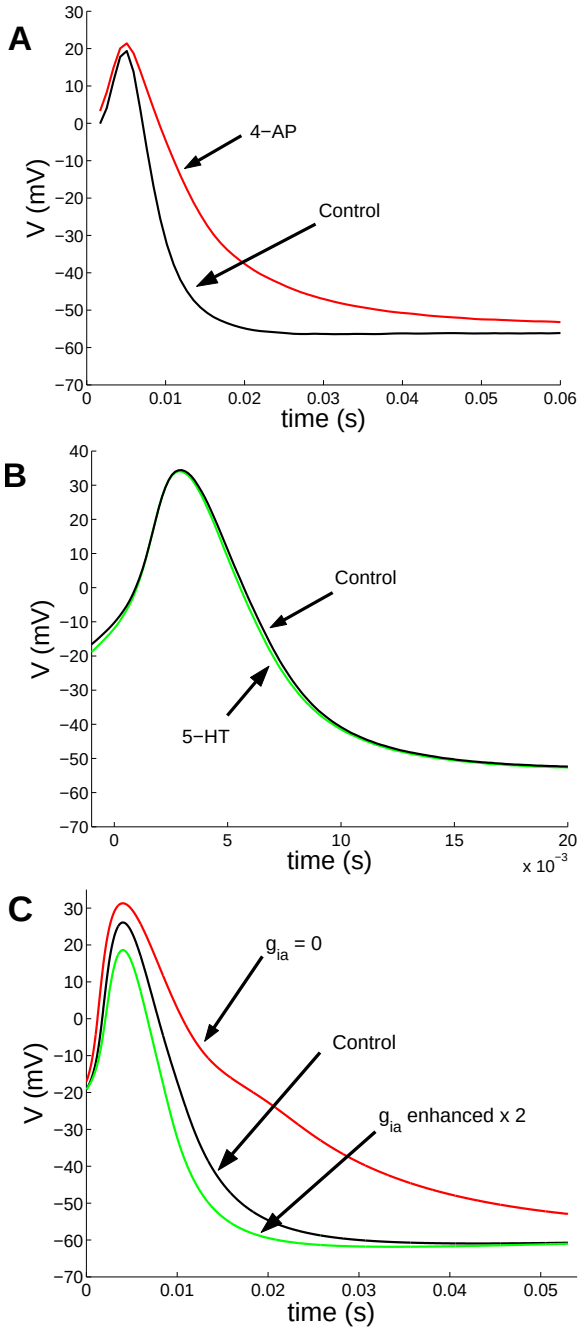

Figure 15: *Comparing the effect of enhanced and depressed g_A on action potential shape in experiments and model. A,* Experimental effect of 4-AP on spike shape. 4-AP, a potassium channel blocker, leads to spike broadening. *B,* Experimental effect of 5-HT on spike shape. 5-HT, which enhances $\overline{g}_A$, slightly decreases the area under the action potential. *C,* The effects of reducing g_A to zero and enhancing it by a factor of two on action potential shape in simulation. The model mimics the broadening effect of 4-AP, with an applied I_{bias} to rectify the resting potential, as well as the spike narrowing due to an enhanced g_A.

the application of 5-HT. The simulations predict a reduction in spike area of 5% for $\overline{g}_A$ increased by 20% (see figures 15 and 17).

The model initially did not match empirical observations, and predicted an increase in area inferior to 60% when g_A was set to zero. To achieve a better match, the maximal conductance and time constants of the delayed rectifier were adjusted until a 91% increase in area was realized when $\overline{g}_A$ is set to zero. The A-current has a significant impact on spike shape and in the repolarization of the action potential in experiments (as can be seen in figure 15A). Yet at first, the A-current was much weaker than the delayed rectifier, and hence spike shape did not change significantly when A-current was removed. This problem was partially solved by reducing the maximal conductance of the delayed rectifier ($\overline{g}_{kd}$), so that the A-current had a significant function in shaping the action potential. If $\overline{g}_{kd}$ was reduced too much, the action potential could not repolarize when $\overline{g}_A$ was set to zero, which set a lower bound to to $\overline{g}_{kd}$. Also, increasing the delayed rectifier time constants slowed the repolarization phase of the action potential, hence widening the pulse.

A side-effect of 4-AP in the VSI-B cell is to depolarize its resting potential, probably by modifying its leak conductance properties [42]. The modification of resting potential is an additional effect to A-current enhancement which would broaden the spike shape. Reducing $\overline{g}_A$ in the model to zero does not have a significant effect on resting potential and increasing its leak would not result in an increased resting potential as $E_{leak} = -54.5$ mV. Hence a constant bias current was introduced to modify resting potential (I_{bias}), a technique used to correct resting potential in [2]. Varying I_{stim} has the same effect as shifting the reversal potential of the leak conductance (E_{leak}). The rectifying I_{bias} changed the percentage increase in area to 100.0% when $\overline{g}_A = 0$ (see figure 17).

After finalizing the model, our goal was to evaluate whether a reduction in spike area of 5% is sufficient to account for the observed EPSC depression during STDN.

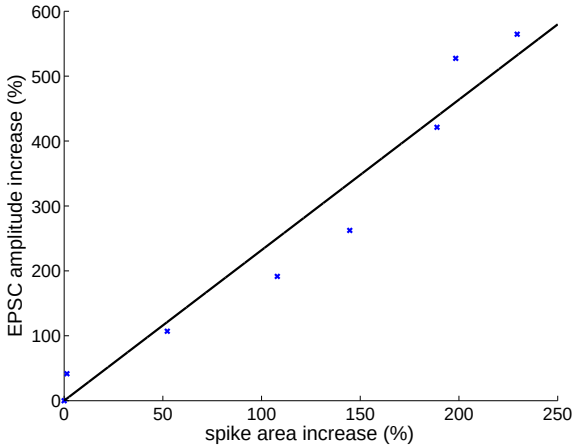

Figure 16: *Relationship between EPSC amplitude increase and spike area increase.* Bath application of 5-HT experiments by Dr. Sakurai enabled us to find the relationship between EPSC amplitude increase and spike area increase. The data points were fitted with a line through the origin. Though this data is based on (n=1), two other preparations showed a similar linear relationship between EPSC amplitude and spike width. The spike area could not be measured because of the stimulus artifacts present in the spikes.

We must first find how the amplitude of the EPSC varies with changes in spike area. Studies have shown an approximately linear change in postsynaptic potential with change in spike duration [36, 45]. Sakurai conducted experiments to find the constant of proportionality for VSI-B, by bath applying 4-AP and measuring spike shape and evoked EPSC amplitude as 4-AP concentration gradually increased in the bath. The level of blocked A-current increases as the pharmacological blocker slowly mixes in with the saline bath solution, and so the effect of 4-AP is not immediate. We plotted area under spike (normalized to control area) versus normalized EPSC amplitude and fitted these points to a line, from which we extracted a constant of proportionality $k = 2.32$ (where EPSC amplitude percentage increase = k $\cdot$ spike area percentage increase), as shown in figure 16.

Relating spike area to EPSC amplitude allows us to find a corresponding relationship between EPSC amplitude and $\overline{g}_A$ conductance change. From figure 17, we can predict that the change in spike shape due to serotonin depresses the EPSC by

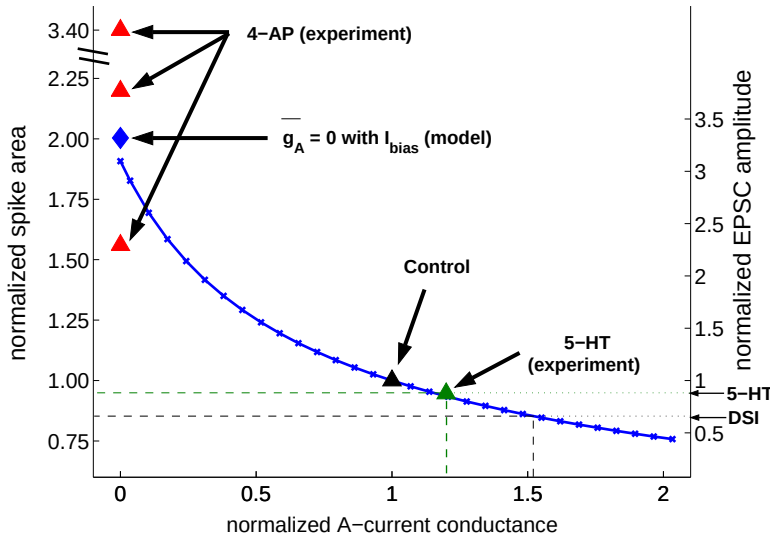

Figure 17: *Effect of change in $\overline{g}_A$ on spike shape.* We conducted a sweep of $\overline{g}_A$ from zero to double the control conductance value while eliciting single action potentials with a brief high-current stimulus (15 Experimental evidence has suggested that nA for 6 nS). The area of the action potential (above a threshold of -20 mV) was calculated and plotted against $\overline{g}_A$ normalized to control. The blue diamond represents the normalized spike area of a simulated spike with $g_A = 0$ and applied $I_{bias} = 1$ nA. The red triangles show the amount of spike change with bath-applied 4-AP. The green triangle shows the amount of spike change with application of 5-HT, with a measured conductance increase of 20%.The linear relationship between percent increase in spike area and EPSC amplitude increase was used to add a second y-axis to the plot, which enables us to extract the percentage of EPSC depression solely due to the enhancement of the A-current due to 5-HT (12.4% - green dashed box). An increase in A-current conductance of 53.8% would be necessary for the observed EPSC depression of 35% caused by DSI stimulation (black dashed box).

approximately 12.4%. The amount of depression observed in response to DSI stimulation is 35%. Therefore, the model predicts that the DSI stimulation would need to decrease the spike area by 15.1% and increase the A-current conductance by 53.8% in order to account for the observed depression.

4.6 Investigating the depression dynamics of STDN

In this section, we will use the VSI-B model to determine whether the inactivation of the A-current is a feasible mechanism for the decreased depression observed during a spike train of VSI-B evoked EPSCs (see section 2.2 and figure 4). If the A-current plays a role in the depression phase of STDN, its inactivation would lead to less spike narrowing, and hence a reduction in the synaptic depression. We can use the model to study the amount of A-current conductance decrease during a VSI-B spike train simulation.

The sole significant feature we can observe in the voltage trace of the evoked spike train is that the amplitude and area of the first spike is larger compared to the rest of the spikes (see figure 18A). The large area of the first spike is due the membrane potential at which the first spike is initiated being higher than the membrane potential at which the subsequent spikes are initiated, which is slightly hyperpolarized due to the post-repolarization hump of the previous spike.

By measuring the peaks of the g_A transient traces during a VSI-B spike train with an enhanced $\overline{g}_A$, we quantified the decrease in A-current. The peak spike conductance decreases with the progression of the spike train (see figure 18). When $\overline{g}_A$ is enhanced by a factor of two, the peak conductance of the tenth spike is 8.8% lower than that of the first spike. The decrease in peak conductance when $\overline{g}_A$ is not enhanced is 12.3%. Thus there is less decrease in A-current conductance when g_A is enhanced than when g_A is not enhanced.

The effect of this slight decrease in g_A on spike shape can be quantified using the

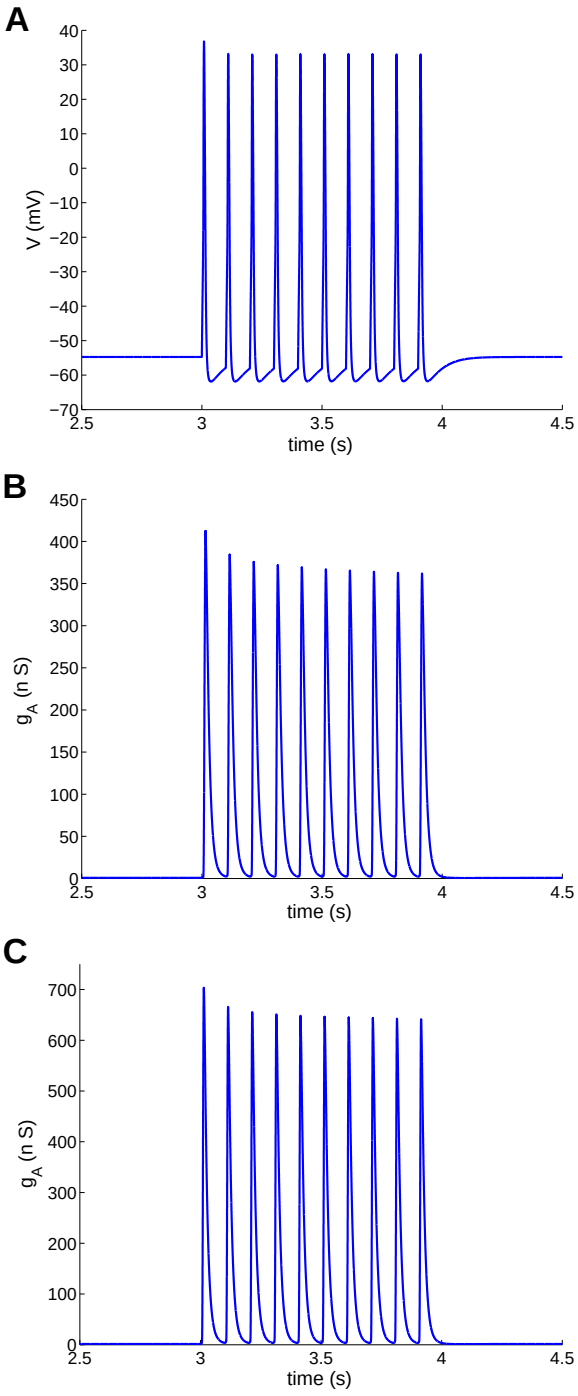

Figure 18: *Voltage and conductance simulation response to spike train stimulation. A,* This plot shows a voltage trace from simulation of ten stimulus pulses (17 nA, 9 nS, 10 Hz), beginning at $t = 3$ s. Shown for $\overline{g}_A$ enhanced by factor of two. *B,* g_A is calculated and recorded from the same simulation as panel A, for non-enhanced $\overline{g}_A$. *C,* Same as B, with for $\overline{g}_A$ enhanced by factor of two over the nominal value.

same metric as presented previously to measure spike shape (area under spike above a threshold of -20 mV). Figure 19 shows the spike area normalized to the area of the first spike. The initial decrease is due to the initial membrane potential of the first spike. As expected from the observed decrease in g_A for spikes 2–10, the spike area increases, though only slightly. From our previously extracted relationship between EPSC and spike shape, we predict that the change in EPSC due to the change in spike area from the second to tenth spike is 2.8%, such a small change is not be sufficient to account for the loss of depression observed in experiments.

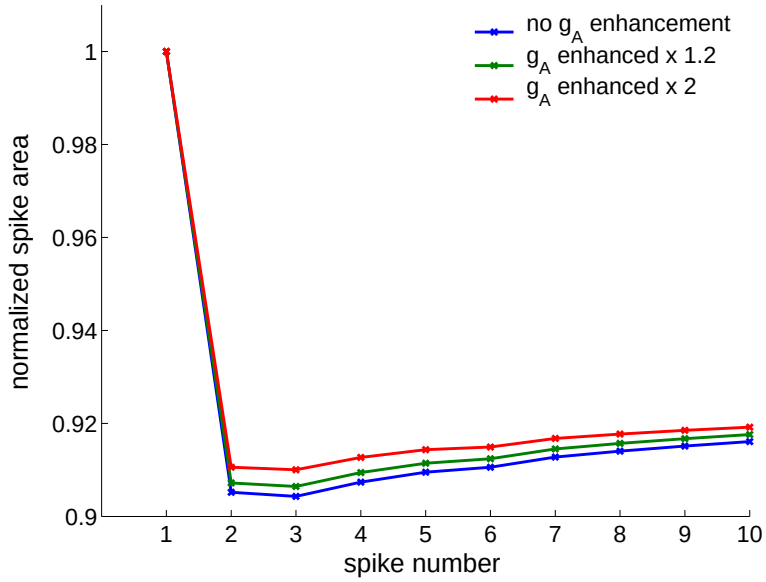

Figure 19: *Increase in spike area with progression of spike train.* The area of the spike over -20 mV is plotted against spike number from elicited spike train shown in figure 18 for three levels of enhancement of $\overline{g}_A$ (not enhanced, enhanced by 20% to mimics effect of 5-HT, and enhanced by 100%). From the plot, we see that there is only a small amount of spike area increase after the second spike. We also observe that the amount of A-current conductance enhancement does not have a significant effect on change in spike area with the advance of the VSI spike train.

CHAPTER V

CONCLUSIONS AND DISCUSSION

We have developed a conductance-based model of a neuron intrinsic to the CPG controlling swimming in *Tritonia diomedea* and its A-current. Simulations using our model demonstrate an accurate representation of the essential electrical properties of the VSI-B, including spike shape, tonic firing properties, resting potential, and resting input conductance. The A-current, based on electrophysiology data acquired intracellularly by Dr. Sakurai, reproduces the amplitude and complex dynamics of the A-current, displayed in the voltage clamp simulations (see figure 12).

Using the model, we tested the hypothesis that the A-current plays a role in the depression phase of STDN. The model predicted the empirically observed amount of spike narrowing with the bath-application of 5-HT, which increases $\overline{g}_A$ by 20%. This indicates that it is feasible for the spike narrowing observed to be due an increase in $\overline{g}_A$. Using experimental data to find the relationship between spike shape and EPSC amplitude, the model predicts a depression in EPSC of 12% due to the increasing of $\overline{g}_A$ effect of 5-HT. As the maximum depression observed during STDN was found to be 35% in experiments [43], we conclude from the model that spike narrowing due to 20% enhanced A-current is not sufficient to account for the depression in STDN.

Though this could imply that there might be other mechanisms which result in a decrease in neurotransmitter release, as with presynaptic facilitation mechanisms in *Aplysia*, we believe that there is a simpler explanation which would account for the disparity between simulated and experimental depression. We think that there is a greater density of serotonin receptors concentrated at the presynaptic terminals of VSI-B, as suggested by experiments where application of 5-HT has led to spike failure

of some back-propagated action potentials and by previous studies which have found an unequal distribution of serotonin receptors, such as in reference [39]. A number of studies have shown that A-current can be been responsible for spike failure [37, 10, 11]. Hence if serotonin receptors are densely localized away from the soma, where the currents are being measured, then their modulation of the A-current channels would be greater in the terminals than in the soma. Our model predicts a depression of 35% in the VSI-B–evoked EPSCs for a 54% enhancement in A-current conductance(see figure 16), the level observed experimentally in STDN [43], which shows proof of concept that an increase in $\overline{g}_A$ can account for the observed depression.

Additionally, we used our model to test whether a reduction in A-current could be responsible for the empirical reduction in depression during a spike train of VSI-B-evoked EPSCs. Using the model, we are able to record the amount of A-current during an evoked spike-train simulation. The results showed a minor inactivation of the A-current, a 9.9% decrease in g_A. Also, we calculated a 0.9% increase in spike area from the second to tenth spike, translating to a 2.0% decrease in EPSC. These results indicate that the inactivation of the A-current is probably not involved in the decreased depression with the advance of the spike train. Further experiments are needed to develop an alternate theory about the dynamics of depression in STDN.

One of the principal aspects of the model is the A-current, as we are interested in the effect of its modulation by 5-HT. The model was based on leak-subtracted data from control experiments and experiments with 4-AP. Hence, we assume that 4-AP is a perfect blocker of solely the A-current and that it does not have any side effects (such as on the health of the living cell). Yet it unlikely that 4-AP is a full A-current blocker, leading to a A-current which is weaker in the model than physiologically. Also, if the 4-AP blocks the delayed rectifier potassium current weakly, then some of the delayed rectifier is "double-counted" as it is being modeled independently. We do not expect these issues to change the results significantly, as the delayed rectifier

maximal conductance was adjusted to fit the firing pattern and effect on spike shape. Therefore, a slightly weaker $\overline{g}_{Kd}$ in the model than physiologically present would correct the fact that the a weak delayed rectifier is included in the A-current model.

The A-current model does not reproduce the full delay-stimulus relationship described in Getting (1983) because the model's parameter space is restricted (or "tight") [14]. Low current stimuli which produce a prolonged delay in tonic firing simulations would lead to shorter delays with the addition of a small amount of experimental noise on the current stimulus. Small depolarizations due to this noise could result in earlier firing and hence smaller delays. The parameter space of the VSI-B model using Getting's A-current model (in section 4.1) was not as restricted. This is not a general trend, since often, models with lower number of parameters and simpler dynamics have "tighter" parameter spaces.

The main assumptions and limitations to the VSI-B model are the modeled sodium and delayed rectifier currents, for which pharmacological blockers do not achieve a full block of channel current. Thus we were not able to base the current dynamics of the sodium and delayed rectifier currents on physiological data from *Tritonia*, since we do not have voltage clamp data for these currents. This adds uncertainty to our VSI-B model and the conclusions drawn from simulations. Another limitation to our conclusions drawn is our metric to measure spike shape. We assume that VSI-B spike area above a threshold of -20 mV is proportional to EPSC amplitude in the post-synaptic cell VFN. Though this metric is based on physiological mechanisms (-20 mV is the approximate threshold for Ca^{2+} influx which leads to neurotransmitter release), a more accurate method for measuring amount of neurotransmitter release would be to explicitly model calcium concentrations and a calcium current in VSI-B, which would enable us to more accurately predict amount of EPSC depression due to change in spike shape. These assumptions and limitations in our model point to the fact that neuronal models are never fully physiologically accurate, and that

models cannot prove hypotheses. Yet models can provide evidence of feasibility of hypotheses, as with this study.

Future modeling work could include the addition of second messenger cascades to the VSI-B, a more complex modeled morphology, and the development of additional CPG neuron models to simulate the full escape swim CPG. Modeling second messenger cascades' interactions with electrical neuronal activity, as in Yu et al. (2004), could test suggested mechanisms enhancing the A-current on neurotransmitter release machinery [49]. If experiments reveal more detailed information on the morphology of the VSI-B and the location of action potential generation (it is thought not to be in soma), our current model could be extended into a multi-compartment model in the NEURON simulation environment. By varying the density of A-current channels to be selectively localized in the terminals, we could test how much A-current increase is needed to display a 20% increase of A-current in the soma. Another potential use of this model in future modeling studies is its incorporation into a physiologically accurate model of the entire escape swim CPG. Again, the NEURON simulation environment is an appropriate platform to construct this network model. In order to export our VSI-B model into a CPG network model, we will need to modify the activation and inactivation curves, as our VSI-B model models high-divalent saline conditions, which shifts the activation curves to the rights, and raises the threshold of firing and reduces spontaneous firing of neurons [43].

To conclude, this study fits in the interdisciplinary research areas (quantitative electrophysiology and neurophysiology) whose goal is to understand the complexities and mechanisms of neuromodulation and synaptic plasticity, which is thought to have a role in learning and memory and biological signal processing pathways throughout the nervous system [5]. By studying neuromodulation and its function in CPGs of less complex animal brains (such as that of invertebrates), we can discover the basic mechanisms underlying CPGs, which are ubiquitous in the nervous system of most

animals, including humans. In this study, we have examined a hypothesis for the mechanism for the depression phase of a complex spike-time-dependent neuromodulation. As with presynaptic facilitation in *Aplysia*, empirical evidence has suggested that modulation of a potassium current is responsible for an observed depression. The conductance of potassium channel currents, which play an important role in the repolarization phase of action potentials in neurons, is crucial to the spike shape and width, which in turn determines amount of neurotransmitter release. Modulation of this conductance can change the synaptic strength of this neuron, and hence plays an important role in neuromodulation. These results suggest that for STDN in *Tritonia*, an enhancement in A-current conductance could be responsible for the depression observed in experiments. Furthermore, our simulations suggest that the inactivation of A-current is not responsible for the dynamics of STDN.

APPENDIX A

MODEL PARAMETERS

A.1 Initial A-current model

Adapted from Getting [15]

$$I_A = \overline{g}_{Na} \cdot m \cdot h \cdot (V - E_K)$$

$$\frac{dm}{dt} = \frac{m_\infty(V) - m}{\tau_m(V)}$$
$$\frac{dh}{dt} = \frac{h_\infty(V) - h}{\tau_h(V)}$$

$$V_{half(m)} = -40 \ mV$$
$$S_{half(m)} = -5.5 \ mV$$
$$\tau_m = 10 \ ms$$
$$V_{half(h)} = -50 \ mV$$
$$S_{half(h)} = 2 \ mV$$
$$\tau_h = 660 \ ms$$

A.2 Parameters for new VSI-B model

The parameters for the A-current model are shown in table 1. The VSI-B was modeled as a single compartment in the NEURON simulation environment with length and diameter of 300 μm. The equations for the A-current, delayed rectifier potassium, fast sodium, and leak currents are the same form as the original Hodgkin-Huxley squid axon model [25]:

$$\begin{aligned} I_A &= \left(\overline{g}_{A1} \cdot {m_A}^4 \cdot h_1 \cdot + \overline{g}_{A2} \cdot {m_A}^4 \cdot h_2 \cdot\right)(V - E_K) \\ I_{Kd} &= \overline{g}_{Kd} \cdot n^4 \cdot (V - E_K) \\ I_{Na} &= \overline{g}_{Na} \cdot {m_{Na}}^3 \cdot h \cdot (V - E_{Na}) \\ I_{leak} &= \overline{g}_{leak} \cdot (V - E_{leak}) \end{aligned}$$

I_A, A-current; I_{Kd}, delayed rectifier potassium current; I_{Na}, fast sodium current; I_{leak}, leak current; $\overline{g}_{A1}$, $\overline{g}_{A2}$, A-current maximal conductances; $\overline{g}_{Kd}$, delayed rectifier potassium maximal conductance; $\overline{g}_{Na}$, fast sodium maximal conductance; m_A, m_{Na}, n, activation state variables; h, h_1, h_2, inactivation state variables; E_K, potassium reversal potential; E_{Na}, sodium reversal potential; E_{leak}, leak reversal potential.

The gating variables $m(t)$, $n(t)$, and $h(t)$ are described by the differential equations:

$$\begin{aligned} \frac{dm}{dt} &= \frac{m_\infty(V) - m}{\tau_m(V)} \\ \frac{dn}{dt} &= \frac{n_\infty(V) - n}{\tau_n(V)} \\ \frac{dh}{dt} &= \frac{h_\infty(V) - h}{\tau_h(V)} \end{aligned}$$

m_∞, n_∞, and h_∞ are described by:

$$\begin{aligned} m_\infty &= \frac{1}{1+e^{\frac{V-V_{half}}{S_{half}}}} \\ n_\infty &= \frac{1}{1+e^{\frac{V-V_{half}}{S_{half}}}} \\ h_\infty &= \frac{1}{1+e^{\frac{V-V_{half}}{S_{half}}}} \end{aligned}$$

The time constants τ_m, τ_n, τ_h (for I_{Na}), τ_{h1} (for I_A), and τ_{h2} (for I_A) are:

$$\begin{aligned} \tau_m &= \tau_{min} + (\tau_{max} - \tau_{min}) \frac{1}{1+e^{\frac{V-\tau_{half}}{S_{half}}}} \\ \tau_n &= \tau_{min} + (\tau_{max} - \tau_{min}) \frac{1}{1+e^{\frac{V-\tau_{half}}{S_{half}}}} \\ \tau_h &= \tau_{min} + (\tau_{max} - \tau_{min}) \frac{1}{1+e^{\frac{V-\tau_{half}}{S_{half}}}} \\ \tau_{h1} &= \tau_{min} + (\tau_{max} - \tau_{min}) \frac{1}{1+e^{\frac{V-\tau_{half}}{S_{half}}}} \\ \tau_{h2} &= \left(\frac{a_1}{1+e^{\frac{(V-V_{half1})}{S_{half1}}}} + \frac{a_2}{1+e^{\frac{(V-V_{half2})}{S_{half2}}}} \right)^{-1} \end{aligned}$$

	τ_{min} (ms)	τ_{max} (ms)	a_1 (ms^{-1})	V_{half} (mV)	S_{half} (mV)	a_2 (ms^{-1})	V_{half2} (mV)	S_{half2} (mV)
m_∞	-	-	-	-33	-14.1	-	-	-
h_∞	-	-	-	-41.4	5.8	-	-	-
τ_m	4	40	-	-19.5	5.3	-	-	-
τ_{h1}	30	110	-	-14	9.0	-	-	-
τ_{h2}	-	-	1.447×10^{-3}	8.3	-2.8	1.580×10^{-3}	-11.7	12.1

Table 1: *Parameters for the A-current model.* The h_∞ parameters are both for h_1 and h_2.

The maximal conductances for the A-current are $\overline{g}_{A1} = 0.369$ μS; $\overline{g}_{A2} = 0.493$ μS. The total membrane capacitance of the neuron (C_m) is 2.83 nF (unit capacitance is 1 μF/cm^2).

	E_r (mV)	$\overline{g}$ (μS)	$V_{half(act.)}$ (mV)	$S_{half(act.)}$	$V_{half(inact.)}$ (mV)	$S_{half(inact.)}$
I_{Na}	50	5.65	-17.5	-7	-27	7
I_{Kd}	-65	0.51	-7	-11.5	-	-
I_{leak}	-54.5	0.0072	-	-	-	-

	τ_{min} (ms)	τ_{max} (ms)	$V_{half(\tau)}$ (mV)	$S_{half(\tau)}$
$\tau_m(Na)$	0.3	-	-	-
$\tau_h(Na)$	3	48	-40	7
$\tau_n(Kd)$	12	92	-30	15

Table 2: Parameters for the delayed rectifier, fast sodium, and leak in the VSI-B model

REFERENCES

[1] Barnes, S., Syed, N., Bulloch, A., and Lukowiak, K., "Modulation of ionic currents by dopamine in an interneurone of the respiratory central pattern generator of *Lymnaea* stagnalis," *Journal of Experimental Biology*, vol. 189, no. 1, pp. 37–54, 1994.

[2] Baxter, D. A., Canavier, C. C., Clark, J. W., and Byrne, J. H., "Computational model of the serotonergic modulation of sensory neurons in *Aplysia*," *Journal of Neurophysiology*, vol. 82, no. 6, pp. 2914–2935, 1999.

[3] Buchholtz, F., Golowasch, J., Epstein, I. R., and Marder, E., "Mathematical model of an identified stomatogastric ganglion neuron," *Journal of Neurophysiology*, vol. 67, no. 2, pp. 332–340, 1992.

[4] Butera, R. J., Clark, J. W., Canavier, C. C., Baxter, D. A., and Byrne, J. H., "Analysis of the effects of modulatory agents on a modeled bursting neuron: dynamic interactions between voltage and calcium dependent systems," *Journal of Computational Neuroscience*, vol. 2, no. 1, pp. 19–44, 1995.

[5] Byrne, J. H. and Kandel, E. R., "Presynaptic facilitation revisited: State and time dependence," *Journal of Neuroscience*, vol. 16, no. 2, pp. 425–435, 1996.

[6] Calabrese, R. L., "Taking the lead from a model," *Current Biology*, vol. 9, no. 18, pp. 680–683, 1999.

[7] Connor, J. and Stevens, C. F., "Prediction of repetitive firing behaviour from voltage clamp data on an isolated neurone soma," *Journal of Physiology*, vol. 213, pp. 31–53, 1971.

[8] Connor, J. and Stevens, C. F., "Voltage clamp studies in a transient outward membrane current in gastropod neuroal somata," *Journal of Physiology*, vol. 213, pp. 21–30, 1971.

[9] Cropper, E. C., Lloyd, P. E., Reed, W., Tenenbaum, R., Kupfermann, I., , and Weiss, K. R., "Multiple neuropeptides in cholinergic motor neurons of *Aplysia*: evidence for modulation intrinsic to the motor circuit," *Proceedings of the Naional Academy of Sciences of the United States of America*, vol. 84, no. 10, pp. 3486–3490, 1987.

[10] Debanne, D., Kopysova, I., Bras, H., and Ferrand, N., "Gating of action potential propagation by an axonal a-like potassium conductance in the hippocampus: A new type of non-synaptic plasticity," *Journal of Physiology (Paris)*, vol. 93, pp. 285–296, 1999.

[11] Debanne, D. and Russier, M., "Axonal propagation: does the spike stop here?," *Journal of Physiology*, vol. 548, p. 663, 2003.

[12] Frankenhaeuser, B. and Hodgkin, A. L., "The action of calcium on the electrical properties of squid axons," *Journal of Physiology*, vol. 137, pp. 218–244, 1957.

[13] Getting, P. A., "Mechanisms of pattern generation underlying swimming in *Tritonia*. II. network reconstruction," *Journal of Neurophysiology*, vol. 49, no. 4, pp. 1017–1035, 1983.

[14] Getting, P. A., "Mechanisms of pattern generation underlying swimming in *Tritonia*. III. intrinsic and synaptic mechanisms for delayed excitation," *Journal of Neurophysiology*, vol. 49, no. 4, pp. 1036–1050, 1983.

[15] Getting, P. A., "A network oscillator underlying swimming in *Tritonia*," in *Neuronal and Cellular Oscillators* (Jacklet, J. W., ed.), ch. 8, New York, NY: Mascei Dekkes Inc., 1989.

[16] Getting, P. A., "Reconstruction of small neural networks," in *Methods in Neuronal Modeling: from Synapses to Networks* (Koch, C. and Segev, I., eds.), ch. 6, Cambridge, MA: MIT Press, 1 ed., 1989.

[17] Gilly, W. F. and Armstrong, C. M., "Divalent cations and the activation kinetics of potassium channels in squid giant axon," *Journal of General Physiology*, vol. 79, pp. 965–996, 1982.

[18] Gilly, W. F. and Armstrong, C. M., "Slowing of sodium channel opening kinetics in squid axon by extracellular zinc," *Journal of General Physiology*, vol. 79, pp. 935–964, 1982.

[19] Gorman, A. L. F. and Mirolli, M., "The passive electrical properties of the membrane of a molluscan neurone," *Journal of Physiology*, vol. 227, pp. 35–40, 1972.

[20] Hahin, R. and Campbell, D. T., "Simple shifts in voltage dependence of sodium channel gating caused by divalent cations," *Journal of General Physiology*, vol. 82, pp. 785–805, 1983.

[21] Harris-Warrick, R. M. in *Neural Control of Rythmic Movements in Vertebrates* (Cohen, A. H., Rossignol, S., and Grillner, S., eds.), pp. 285–331, New York, NY: Wiley Interscience, 1988.

[22] Hines, M. L., "NEURON – a program for simulation of nerve equations," in *Neural Systems: Analysis and Modeling* (Eeckman, F., ed.), pp. 127–136, Norwell, MA: Kluwer, 1993.

[23] Hines, M. L., "The NEURON simulation program," in *Neural Network Simulation Environments* (Skrzypek, J., ed.), pp. 147–163, Norwell, MA: Kluwer, 1994.

[24] Hines, M. L., "The neurosimulator NEURON," in *Methods in Neuronal Modeling: from Synapses to Networks* (Koch, C. and Segev, I., eds.), pp. 121–136, Cambridge, MA: MIT Press, 2 ed., 1998.

[25] Hodgkin, A. L. and Huxley, A. F., "A quantitative description of membrane current and its application to conduction and excitation in nerve," *Journal of Physiology*, vol. 117, no. 4, pp. 500–544, 1952.

[26] Holstege, J. C. and Kuypers, H. G., "Brainstem projections to spinal motoneurons: An update," *Journal of Neuroscience*, vol. 23, no. 3, pp. 809–821, 1987.

[27] Holz, G. G., Shefner, S. A., and Anderson, E. G., "Serotonin decreases the duration of action potentials recorded from tetraethylammonium-treated bullfrog dorsal root ganglion cells," *Journal of Neuroscience*, vol. 6, no. 3, pp. 620–626, 1986.

[28] Huguenard, J. R. and McCormick, D. A., "A model of the electrophysiological properties of thalamocortical relay neurons," *Journal of Neurophysiology*, vol. 68, no. 4, pp. 1373–1383, 1992.

[29] Johnston, D. and Wu, S. M. S., *Foundations of Cellular Neurophysiology*. Cambridge, MA: MIT Press, 2001.

[30] Katz, P. S., ed., *Beyond Neurotransmission: Neuromodulation and its importance for Information Processing*. New York: Oxford University Press, 1999.

[31] Katz, P. S., Getting, P. A., and Frost, W. N., "Dynamic neuromodulation of synaptic strength intrinsic to a central pattern generator circuit.," *Nature*, vol. 367, pp. 729–731, 1994.

[32] Katz, P. S. and Harris-Warrick, R. M., "Actions of identified neuromodulatory neurons in a simple motor system," *Trends in Neuroscience*, vol. 13, no. 9, pp. 367–373, 1990.

[33] Katz, P. S. and Frost, W. N., "Intrinsic neuromodulation in the *Tritonia* swim CPG: Serotonin mediates both neuromodulation and neurotransmission by the dorsal swim interneurons," *Journal of Neurophysiology*, vol. 74, pp. 2281–2294, 1995.

[34] Katz, P. S. and Frost, W. N., "Intrinsic neuromodulation: Altering neuronal circuits from within," *Trends in Neuroscience*, vol. 19, pp. 54–61, 1996.

[35] Klein, M., "Distinct component of presynaptic calcium current is increased by cyclic AMP at *Aplysia* sensorimotor synapses in culture," *Society for Neuroscience Abstracts*, vol. 20, p. 1073, 1994.

[36] Klein, M., "Synaptic augmentation by 5-HT at rested *Aplysia* sensorimotor synapses: Independence of action potential prolongation," *Neuron*, vol. 13, pp. 159–166, 1994.

[37] Kopysova, I. and Debanne, D., "Critical role of axonal A-type K channels and axonal geometry in the gating of action potential propagation along CA3 pyrimidal cell axons: A simulation study," *Journal of Neuroscience*, vol. 18, no. 18, pp. 7436–7451, 1998.

[38] Lennard, P. R., Getting, P. A., and Hume, R. I., "Central pattern gerator mediating swimming in *tritonia*. II. initiation, maintenance, and termination," *Journal of Neurophysiology*, vol. 44, no. 1, pp. 165–173, 1980.

[39] Marinesco, S. and Carew, T. J., "Serotonin release evoked by tail nerve stimulation in the CNS of *aplysia*: Characterization and relationship to heterosynaptic plasticity," *Journal of Neuroscience*, vol. 22, no. 6, pp. 2299–2312, 2002.

[40] McClellan, A. D., Brown, G. D., and Getting, P. A., "Modulation of swimming in *Tritonia*: Excitatory and inhibitory effects of serotonin," *Journal of Computational Physiology*, vol. 174, pp. 257–266, 1994.

[41] Mirolli, M. and Talbott, S., "The geometrical factors determining the electronic properties of a molluscan neurone," *Journal of Physiology*, vol. 227, pp. 19–34, 1972.

[42] Sakurai, A. and Katz, P. S., "4-AP and IBMX selectively block the depression phase of a biphasic neuromodulation of synaptic strength by serotonergic neurons in the *Tritonia* swim CPG," *Neuroscience Abstracts*, vol. 29, no. 168.18, 2003.

[43] Sakurai, A. and Katz, P. S., "Spike timing-dependent serotonergic neuromodulation of synaptic strength intrinsic to a central pattern generator circuit," *Journal of Neuroscience*, vol. 23, no. 32, pp. 10745–10755, 2003.

[44] Satterlie, R. A., Norekian, T. P., and Pirtle, T. J., "Serotonin-induced spike narrowing in a locomotor pattern generator permits increases in cycle frequency during accelerations," *Journal of Neurophysiology*, vol. 83, no. 4, pp. 2163–2170, 2000.

[45] Sugita, S., Baxter, D. A., and Byrne, J. H., "Spike duration-independent processes may contribute to the rapidly developing component of serotonin- and PKC-induced facilitation of nondepressed tail sensory neurons in *Aplysia*," *Society for Neuroscience Abstracts*, vol. 20, p. 815, 1994.

[46] Thompson, S. H., "Three pharmacologically distinct potassium channels in molluscan neurones," *Journal of Physiology*, vol. 265, pp. 465–488, 1977.

[47] Willows, A. O. D., "Behavioral acts elicited by stimulation of single, identifiable brain cells," *Science*, vol. 157, no. 3788, pp. 570–574, 1967.

[48] Willows, A. O. D. and Hoyle, G., "Neuronal network triggering a fixed action pattern," *Science*, vol. 166, no. 3912, pp. 1549–1551, 1969.

[49] Yu, X., Byrne, J. H., and Baxter, D. A., "Modeling interactions between electrical activity and second-messenger cascades in *Aplysia* neuron R15," *Journal of Neurophysiology*, vol. 91, no. 5, pp. 2297–2311, 2004.